remote sensing

MDPI

Article

Enhancing Hydrological Model Calibration for Flood Prediction in Dam-Regulated Basins with Satellite-Derived Reservoir Dynamics

Chaoqun Li [1,2], Huan Wu [1,2,3,*], Lorenzo Alfieri [4], Yiwen Mei [5], Nergui Nanding [6], Zhijun Huang [1,2], Ying Hu [7] and Lei Qu [1,2]

1 School of Atmospheric Sciences, Sun Yat-sen University, and Southern Marine Science and Engineering Guangdong Laboratory (Zhuhai), Zhuhai 519082, China; lichq6@mail2.sysu.edu.cn (C.L.); qulei7@mail2.sysu.edu.cn (L.Q.)
2 Guangdong Province Key Laboratory for Climate Change and Natural Disaster Studies, Sun Yat-sen University, Zhuhai 519082, China
3 Earth System Science Interdisciplinary Center, University of Maryland, College Park, MD 20740, USA
4 CIMA Research Foundation, 17100 Savona, Italy; lorenzo.alfieri@cimafoundation.org
5 Carbon-Water Observation and Research Station in Karst Regions of Northern Guangdong, School of Geography and Planning, Sun Yat-sen University, Guangzhou 510006, China; meiyw3@mail.sysu.edu.cn
6 School of Earth Sciences, Yunnan University, Kunming 650091, China; nanding@ynu.edu.cn
7 Hubei Meteorological Service Center, Wuhan 430074, China
* Correspondence: wuhuan3@mail.sysu.edu.cn

Highlights

What are the main findings?

- A satellite-based reservoir operation scheme is developed and validated to represent dam regulation processes in hydrologic models, and is demonstrated to enhance model calibration results.

What are the implications of the main findings?

- Incorporating reservoir operation into distributed model calibration refines parameterization and enhances basin-internal hydrological process representation, particularly in simulating flood occurrence and timing.
- Conventional calibration excluding dams tends to distort model parameters, leading to misrepresentation of basin-internal hydrological responsive behavior, yielding attenuated flood peaks, prolonged flood recessions, and underestimated dry-season discharges.

Abstract

The construction and operation of reservoirs have made hydrological processes complex, posing challenges to flood modeling. While many hydrological models have incorporated reservoir operation schemes to improve discharge estimation, the influence of reservoir representation on model calibration has not been sufficiently evaluated—an issue that fundamentally affects the spatial reliability of distributed modeling. Additionally, the limited availability of reservoir regulation data impedes dam-inclusive flood simulation. To overcome these limitations, this study proposes a synergistic modeling framework for data-scarce dammed basins. It integrates a satellite-based reservoir operation scheme into a distributed hydrological model and incorporates reservoir processes into the model calibration procedure. The framework was tested using the coupled version of the DRIVE flood model (DRIVE-Dam) in the Nandu River Basin, southern China. Two calibration configurations, with and without dam operation (CWD vs. CWOD), were compared. Results show that reservoir dynamics were effectively reconstructed by combining satellite

Check for updates

Academic Editor: Konstantinos X. Soulis

Received: 27 October 2025
Revised: 29 December 2025
Accepted: 4 January 2026
Published: 6 January 2026

Copyright: © 2026 by the authors. Licensee MDPI, Basel, Switzerland. This article is an open access article distributed under the terms and conditions of the Creative Commons Attribution (CC BY) license.

altimetry with FABDEM topography, successfully supporting the development of the reservoir scheme. Multi-site comparisons indicate that, while CWD slightly improved streamflow estimation (NSE and KGE > 0.75, similar to CWOD) on the calibrated outlet gauge, it enhanced basin-internal process representation, as evidenced by the superior peak discharge and flood event capture with reduced bias, boosting flood detection probability from 0.54 to 0.60 and reducing false alarms from 0.28 to 0.15. The improvements stem from refined parameterization enabled by a physically complete model structure. In contrast, CWOD leads to subdued flood impulses and prolonged recession due to spurious parameters that distort baseflow and runoff response. The proposed methodology provides a practical reference for flood forecasting in dam-regulated basins, demonstrating that reservoir representation enhances model parameterization and underscoring the strong potential of satellite observations for hydrological modeling in data-limited regions.

Keywords: reservoir operation scheme; satellite altimetry; remote sensing; reservoir dynamics reconstruction; distributed hydrological model; parameter calibration; flood prediction; DRIVE

1. Introduction

Over the past few decades, artificial reservoirs have been constructed worldwide [1–3]. While they provide crucial services such as hydropower generation and flood control, reservoirs also fragment river networks [4,5] and alter the timing and distribution of water flows [6–10]. These alterations exacerbate the nonlinearity of water systems and heighten uncertainty in predictions of extreme hydrological events [11,12]. Under the intensifying anthropogenic activities, traditional hydrological models—which are primarily built on natural processes—require essential modifications, such as structural and parameterization advancements, to reconcile discrepancies with reality. This adaptation is a critical step toward improving large-scale hydrological modeling and flood forecasting.

Distributed hydrological models (DHMs) are the dominant model family in watershed flood forecasting and require parameter calibration for operational application [13–17]. Single-site calibration (SSC) is a basic and widely used method that optimizes model parameters by minimizing discrepancies between simulated and observed flows at a hydrologic station [15,18–24]. Capitalizing on DHM's watershed-discretization capability, SSC provides the added benefit of generating optimized flow estimates across upstream multi-areas (subbasins or grid points) using a single gauge [25,26]. Building on this structural advantage, real-time flood forecasting systems at both global and regional scales use DHMs as their core engine to provide comprehensive flood information across large domains [17,27–29]. Moreover, due to the sparse, unevenly distributed gauges globally, downstream flow records have become the de facto basin-wide hydrological proxies for model calibration and evaluation, leading to the prevalence of SSC [15,30].

However, reservoirs pose challenges to the DHM-SSC framework, potentially leading to estimation errors throughout the basin and reducing the model's reliability. The parameters to be optimized are typically from DHM's Land Surface Model component, which generates the hydrological fluxes across the watershed and drives the routing component. This generic structure-parameterization of DHMs is deficient for dammed basins since matching modeled natural flow with observed unnatural (regulated) hydrographs during calibration distorts parameters, inducing not only elevated false alarm rates in downstream flood predictions [17], but also misrepresentation of upstream water conditions, such as surface runoff, infiltration, and baseflow [31]. Alfieri, Bucherie [32] showed that even in operational flood forecasting in well-calibrated catchments, higher uncertain-

ties remain in those with more prominent dam regulation. To tackle these challenges, the hydrological community has developed parameter regionalization approaches that transfer parameters calibrated in small, natural catchments to larger, regulated ones using specific algorithms [33–37]. Yet, as an increasing number of newly constructed reservoirs occupy headwater basins [3,38], these indirect methods will lose advantages, necessitating solutions for direct model calibration.

Integrating reservoir processes into DHMs and including them within the calibration are expected to reduce parameter misestimation. Theoretically, the model's robustness is affected by both its structure and its parameters; a more realistic physical structure facilitates better parameterization. Although numerous reservoir operation schemes (modules) have been developed and integrated into DHMs, which have been comprehensively reviewed by [39], they are designed only for better downstream simulation accuracy through improving the model structure. Few studies have explored the further influences of reservoir representation on model parameterization. Dang, Chowdhury [31] and Zhong, Zhao [40] incorporated the dam regulation into the SSC on the Mekong River and China's Dongjiang basin, respectively, and achieved reduced model error at the downstream calibrated station. Nevertheless, the reliability of the dam-included calibration still lacks comprehensive assessments for distributed simulation, such as flood detection across the basin.

Furthermore, limited data availability constrains reservoir modeling in regulated basins, hindering the spread of dam-included calibration within the community. Reservoir operation schemes rely heavily on operational data for precise modeling. The layered characteristics of reservoir capacity are the key scheme parameters that need to be calibrated against in situ storage time series provided by local management authorities [41–48]. However, across the globe, strategic water resource policies often restrict data access [1,47,49–55]. Even GRanD [56], which may be considered as the most comprehensive global reservoir attribute dataset, cannot provide adequate key parameters [57,58]. Moreover, the GRanD includes only about 7000 large reservoirs globally. In contrast, tens of thousands of small- and medium-sized reservoirs [59,60] lack open-access characteristics when incorporated into high-resolution and regional simulations. Thus, developing a reservoir modeling framework independent of ground-based observations and attribute records is essential.

Advances in satellite observation offer opportunities for reservoir modeling in data-scarce regions. Shen, Yamazaki [58] and Hanazaki, Yamazaki [57] used monthly remotely sensed surface area data to determine parameters in reservoir schemes. Dong, Yang [47] reconstructed daily reservoir storage by integrating 10-day satellite altimetry with DEM-derived bathymetry, enabling parameter calibration for the reservoir module. These studies have shown the potential of remote sensing, yet employed it merely as an auxiliary tool to estimate selected parameters. At the same time, critical reservoir features, such as total capacity, were still derived from the GRanD database. A fully satellite-based reservoir operation scheme remains unrealized but would be invaluable for simulating reservoir dynamics in data-unavailable basins. Yassin, Razavi [43] demonstrated the feasibility of using historical storage statistics to define the prior-knowledge-limited scheme parameters. This suggests that a reservoir scheme could be established by reconstructing high-frequency water dynamics through the integration of satellite altimetry and DEM. Notably, existing studies rely on the outdated SRTM DEM for storage estimation [47,50,52,55], whereas new generation, lower-error DEMs, such as the Forest And Buildings removed Copernicus 30 m DEM FABDEM [61] have yet to be exploited in this context.

This study aims to improve hydrologic model calibration and flood prediction in dam-regulated basins under low-data-availability conditions, focusing on addressing two questions:

(1) How can remote sensing data alone be used to develop a reservoir operation scheme that enhances the accuracy of flow estimation by the DHM at dam sites?
(2) To what extent does incorporating reservoir operations into DHM calibration improve hydrological (flood) estimates across the basin, and what are the associated spatial-temporal effects?

We developed a modeling framework that combines satellite data to reconstruct daily reservoir dynamics and establish a reservoir operation scheme, which was incorporated into the DRIVE [17] hydrological model (termed DRIVE-Dam). DRIVE-Dam was tested using two parameter optimization strategies: calibration with dam (CWD) and calibration without dam (CWOD). Multiple basin-internal hydrological stations were utilized to support the assessment of calibration performance. Furthermore, the mechanistic differences in the rainfall-runoff responsive behavior within the model were analyzed.

2. Study Area

The Nandu River Basin (NRB), Hainan Island's largest river system, was selected for its combination of strong reservoir regulation and recurrent flooding, which aligns with the research aims. This 7176 km^2 basin features a 311 km mainstem [62] with a total elevation gradient of 703 m (Figure 1). The NRB has a tropical monsoon climate, with mean annual temperatures of 22–26 °C and average precipitation of 1914 mm. Distinct seasonal precipitation patterns prevail, with >80% of yearly rainfall concentrated during the May-October wet season. The July–October typhoon-prone period often triggers extreme floods, resulting in severe socioeconomic impacts [63].

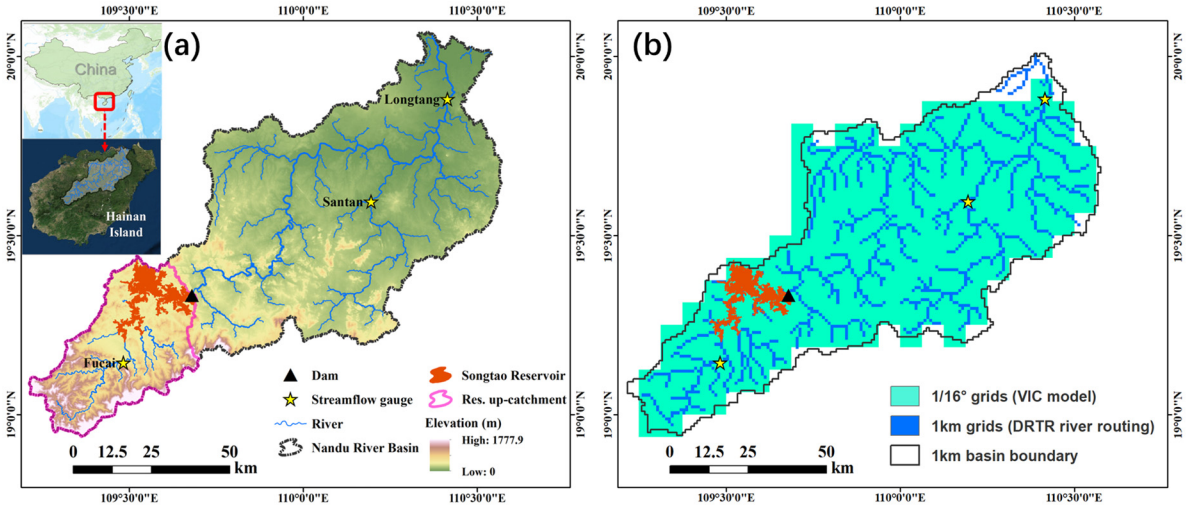

Figure 1. Nandu River Basin. (**a**) Overview of the basin's hydrological and geographical setting. The Songtao Reservoir regulates the mainstem. The Longtang station (downstream) is used for DRIVE-Dam model calibration and validation, while the Santan (unregulated tributary) and Fucai (dam-upstream) stations serve as auxiliary gauges to evaluate calibration performance at internal basin locations. (**b**) Nested runoff–routing resolution configuration of the model grids over the basin.

Located in the NRB's upper reach, Songtao Reservoir serves as the principal hydraulic infrastructure, with a storage capacity of 3.345 billion m^3 [64]. This facility integrates multipurpose operations including flood control, irrigation, municipal water supply, and hydropower generation. Its operational duality involves (1) dry-season prioritization of water allocation for downstream urban-industrial sectors, and (2) wet-season implementation of coordinated flood mitigation through peak shaving and controlled discharge, with strategic impoundment ensuring year-round water security. The dam regulation has significantly altered the spatiotemporal distribution of hydrology, compromising flood

forecasting and emergency response in the urbanized reaches. During the flood season, the Hainan Provincial Meteorological Bureau must assess flood conditions across the entire basin, not just in the downstream areas, to deliver timely early warnings. However, information on reservoir operations is controlled by local water authorities and not shared in real time. This necessitates the development of a dam-inclusive DHM covering the entire basin that integrates satellite data to predict generalized reservoir behavior.

3. Data and Methodology

The proposed modeling framework (as shown in Figure 2) targets a representative DHM calibration situation in a dam-regulated catchment where only downstream flow observations are available for calibration. Reservoir storage time series were first reconstructed using satellite data to establish the reservoir module. A pre-calibration step is designed for the module parameter estimation, after which the DRIVE-Dam can execute the CWD. All simulations were performed on the high-performance computing cluster of the Extreme Hydrometeorology Modeling Team at Sun Yat-sen University. Data processing and statistical analysis were conducted using Python (v3.11.4).

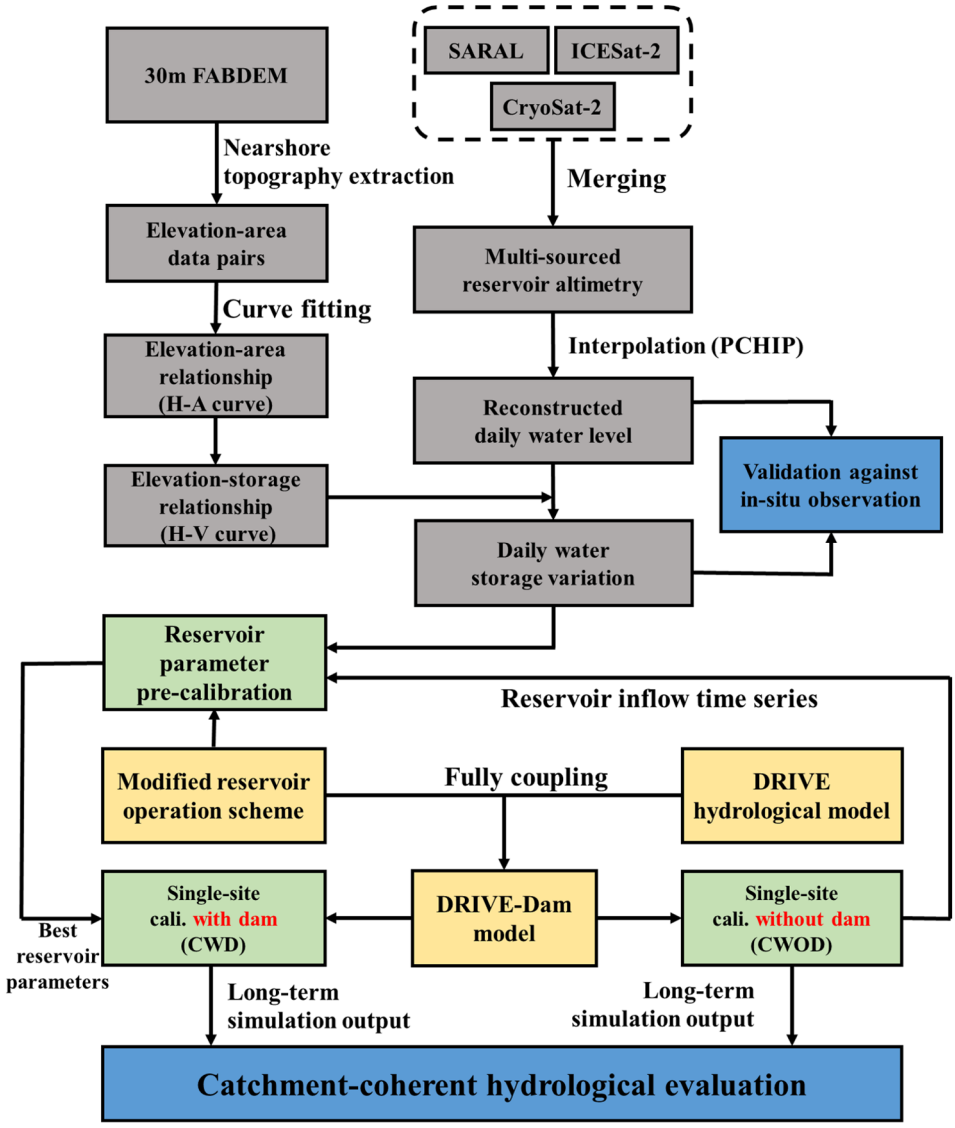

Figure 2. Flowchart representing the methodology and workflow of this study.

3.1. Data Sources

The 1/16° resolution soil, vegetation, and land-cover parameter datasets [65] are used as static inputs to the VIC component of the DRIVE. The DRTR routing component of DRIVE utilizes a 1 km-resolution HydroSHEDS DEM [66] and its derived hydrography maps, including flow direction, flow distance, stream order, slope, and upstream area for each 1 km grid cell. Meteorological forcing data include IMERG V07 Final satellite precipitation [67,68], and MERRA-2 wind speed and temperature, linearly resampled to 1/16° resolution matching the VIC spatial mask, at daily temporal intervals. Daily streamflow observations (2004–2017) were obtained from three hydrological stations, which are illustrated in Figure 1.

The altimetry data of Songtao Reservoir (2011–2021) were obtained from the multi-source fused and enhanced satellite product published by Shen, Liu [69], including 104 points (average interval: 39.8 days; range: 2–198 days) based on measurements from SARAL (29 days), CryoSat (57 days), and ICESat-2 (18 days) satellite. The 30 m resolution FABDEM was employed to extract reservoir slope topography for deriving water level-area-volume (H-A-V) relationships, as it demonstrates high vertical accuracy globally [61,70]. In situ daily water-level and storage records (2015–2021) from the reservoir authority were used to validate the satellite altimetry interpolation and the reconstructed storage variation. All datasets used in this study are listed in Table 1.

Table 1. Summary of datasets used in this study, including model inputs, meteorological forcings, and validation data.

Category	Dataset/Variable	Spatial Resolution	Temporal Resolution/Period	Source
Model static parameters	Soil, vegetation, and land-cover parameters for VIC	1/16°	Static	Schaperow et al. [65]
	HydroSHEDS DEM and derived hydrography (flow direction, flow distance, stream order, slope et al.)	1 km	Static	Lehner et al. [66]
Meteorological forcings	Precipitation (IMERG V07 Final)	0.1° (resampled to 1/16°)	Daily (2004–2021)	NASA [67,68]
	Wind speed and air temperature (MERRA-2)	0.5° × 0.625° (resampled to 1/16°)	Daily (2004–2021)	NASA GMAO
DEM	FABDEM (reservoir topography for H–A–V extraction)	30 m	Static	Hawker et al. [61,70]
Reservoir altimetry	Multi-source fused reservoir water level (Songtao Reservoir)	Point-scale (virtual station)	Irregular (avg. 39.8 days); 2011–2021	Shen & Liu [69]; SARAL, CryoSat, ICESat-2
In situ observations	Streamflow discharge	Point-scale (3 stations)	Daily (2004–2017)	Hainan Provincial Meteorological Bureau
	Reservoir water level and storage	Point-scale	Daily (2015–2021)	Reservoir management authority

3.2. DRIVE-Dam Hydrological Model Framework

3.2.1. DRIVE Model

We used the DRIVE distributed hydrological model as the base model to couple the reservoir scheme and perform calibration experiments. DRIVE was developed for large-scale flood simulation [17]. It integrates the VIC model [71] with advanced land-surface flux simulation capabilities and the DRTR routing model, featuring adaptable river-network parameterization across different scales [72,73], thereby enabling flexible multi-scale flood monitoring and forecasting [74]. DRIVE has long served as the core of the Global Flood Monitoring System (GFMS), with resolutions of 1 km and ~12 km (http://flood.umd.edu (accessed on 30 December 2025)). Also, it supports flood simulation and related analyses at local scales [74,75]. The DRIVE model is well-suited for this study because its VIC component is a typical land surface model that requires calibration. While Jiang and Wu [76] employed DRIVE for calibration methodology research; their study did not account for reservoir effects. In this study, we adopted a nested-grid configuration, with the VIC operating at a 1/16° resolution and the DRTR routing at a 1 km resolution, extracting baseflow and runoff from the corresponding 1/16° VIC cell. The spatial distribution of the nested-resolution grid cells over the basin is shown in Figure 1b.

3.2.2. Development and Coupling of Reservoir Scheme in DRIVE

We developed a parametric reservoir operation scheme to explicitly represent the reservoir storage-release process within the DRIVE model. This scheme builds upon the approach used in LISFLOOD Scheme [77], which vertically partitions the storage capacity into operational zones and estimates the dam release by a piecewise function. The LISFLOOD Scheme is a prevailing paradigm in reservoir modeling, with numerous derived variants demonstrating robust capabilities in capturing reservoir storage dynamics [43,47,57,78]. Our proposed reservoir scheme aims to estimate the outflow, which first satisfies the mass conservation equations:

$$\frac{\Delta V}{\Delta t} = \overline{Q_{in}} - \overline{Q_{out}} + \overline{P} - \overline{E} \tag{1}$$

$$\frac{V_{t+1} - V_t}{\Delta t} = \frac{Q_{in_{t+1}} + Q_{in_t}}{2} - \frac{Q_{out_{t+1}} + Q_{out_t}}{2} \tag{2}$$

where $\overline{Q_{in}}$ and $\overline{Q_{out}}$ represent reservoir's inflows and outflows, respectively. $\overline{P}$ and $\overline{E}$ represent precipitation and evaporation, respectively, which are vertical fluxes and are already included in the land-surface flux calculations within the VIC model. Equation (2), expressed in finite difference form of Equation (1), uses subscripts t and $t + 1$ to denote the current and next model time steps, respectively, in which V_t (water storage of the last step) $Q_{in\,t}$, $Q_{in\,t+1}$ and $Q_{out\,t}$ are known while V_{t+1} and $Q_{out\,t+1}$ are unknown. The $Q_{out\,t+1}$ subsequently determined by Equation (3a), which represents the generic operation rule of a reservoir with four operational zones and three characteristic storage volumes (the conceptual diagram is shown in Figure 3):

$$Q_{out} = \begin{cases} \min\left(\frac{V_t}{\Delta t}, Q_{min}\right) & (V_t \le V_d) \\ Q_{min} + (Q_n - Q_{min}) \cdot r_1 & (V_d < V_t \le V_c) \\ Q_n + \max\left(Q_{in} - Q_n,\ Q_f - Q_n\right) \cdot r_2 & \left(V_c < V_t \le V_f\right) \\ \max\left(\frac{V_t - V_f}{\Delta t}, Q_f\right) & \left(V_t > V_f\right) \end{cases} \tag{3a}$$

$$r_1 = exp\left[-10 \cdot \left(\frac{V_t - V_d}{V_c - V_d} - k\right)^2\right] \tag{3b}$$

$$r_2 = exp\left[-10 \cdot \left(\frac{V_t - V_c}{V_f - V_c} - k\right)^2\right] \quad (3c)$$

where V_d, V_c, and V_f (m^3) represent the water storage volumes corresponding to the dead storage level, conservation level, and flood control level, respectively. In this study, V_d, V_c, and V_f were determined via satellite-derived water storage time series (see details in Section 3.3.2) as they are usually not included in publicly available data. Q_{min}, Q_n, and Q_f ($m^3\ s^{-1}$) denote the minimum required flow, normal flow, and non-damaging downstream flow, respectively, and are estimated based on simulated inflow. In Equation (3b,c), r_1 and r_2 represent the nonlinear control factors for reservoir outflow when the water storage falls within the two intermediate operation zones. The parameter k determines their response to the storage filling ratio and needs to be calibrated within the range of 0–1. The calibration range of and results of these six static parameters (V_f, V_c, V_d, Q_f, Q_n and k) are detailed in Table S1. All storage-related variables are expressed in cubic meters (m^3), flow variables in cubic meters per second ($m^3\ s^{-1}$), and the model time step Δt equals 86,400 s (daily time step).

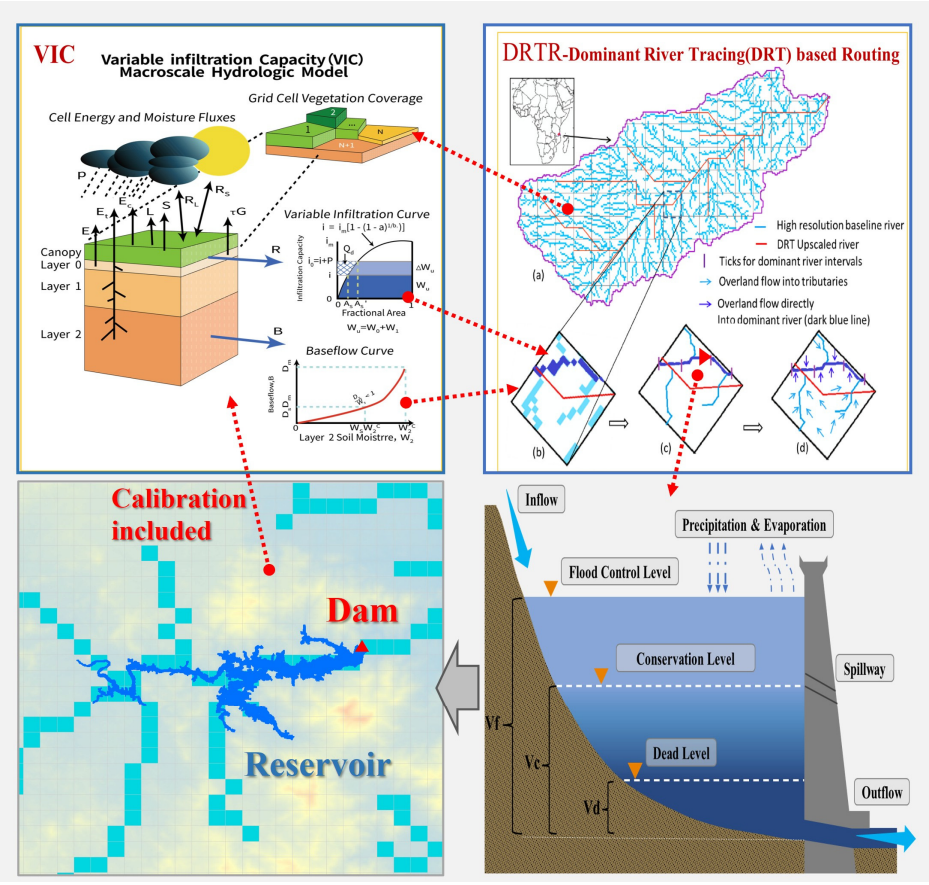

Figure 3. Schematic of the coupled DRIVE-Dam Model. The **upper** panels display the original DRIVE model structure, which integrates the VIC and DRTR models. The **lower** panels illustrate the layered design of the reservoir operation scheme and grid-cell-based implementation within DRIVE. V_d, V_c, and V_f represent the characteristic water storage parameters corresponding to the dead storage level, conservation level, and flood control level, respectively.

When storage falls below the dead storage level ($V_t < V_d$), releases are restricted to the minimum required flow (Q_{min}) to sustain downstream ecological integrity. For water volume between the dead storage and conservation levels ($V_d \leq V_t < V_c$), releases prioritize meeting normal downstream water demands (Q_n), ensuring efficient water use

and maintaining long-term water availability. When storage is between the conservation and flood control levels ($V_c \leq V_t < V_f$), releases aim to maintain non-damaging downstream flow (Q_f), balancing downstream safety with precautionary flood storage capacity. When storage reaches or exceeds the flood control level ($V_t \geq V_f$), the reservoir increases releases to reduce storage and mitigate flood risks rapidly.

The key adjustment in our proposed scheme, compared to the original LISFLOOD Scheme, lies in the modification of storage filling ratio multipliers $\frac{Vt-Vd}{Vc-Vd}$ and $\frac{Vt-Vc}{Vf-Vc}$ when $V_d \leq V_t < V_f$. In the LISFLOOD Scheme, these multipliers are linear functions of V_t. This tends to result in excessively rapid storage drawdown during the post-flood period. In practical reservoir management in China, outflows during this period are carefully regulated to maintain adequate storage and ensure a continuous water supply throughout the forthcoming dry season. We adjusted the multipliers to nonlinear terms r_1 and r_2 to address this issue. The parameter k adjusts the responses of r_1 and r_2 to the filling ratio, enabling optimal alignment with real variation. To compare the robustness of the two schemes, supplementary calibration experiments were conducted across 11 large-scale reservoirs in mainland China. These simulations were driven by observed inflows, with observed storage serving as the calibration benchmark. The results indicate that the parameter k in our scheme is reservoir-specific and significantly influences response characteristics. Overall, DRIVE-Dam demonstrated superior performance compared to the LISFLOOD scheme, particularly during the drawdown phase (Figure S2 and Table S2). In this study, the optimized k on Songtao Reservoir is 0.607.

The proposed reservoir scheme (Equations (2) and (3)) was fully integrated into the DRIVE model (hereafter referred to as DRIVE-Dam), in which each reservoir is simplified as a dam grid cell in the routing scheme, replacing the original river cells, and provides the estimated dam outflow for downstream flow simulation (Figure 3).

3.3. Satellite-Based Reservoir Storage Reconstruction

3.3.1. H-A-V Relationship Extraction from FABDEM

Estimating and calibrating the reservoir module's storage parameters (V_d, V_n, V_f) requires water storage time series. Since in situ storage could not be directly measured, it must be inferred from observable water-level and surface-area data. Previous approaches relied on pairing water levels (H) from satellite altimetry with surface areas (A) from optical imagery using temporally matched remote sensing data—a method often compromised by cloud contamination and data gaps [49,79–81]. In this study, we adopted a workflow similar to that of Dong, Yang [47] for accurate reconstruction of daily water levels from satellite altimetry data. Then, daily storage volumes (V) were derived using a water elevation-area-storage (H-A-V) relationship, defined from high-quality topographic data, thereby circumventing the limitations of methods based on satellite imagery.

The H-A-V extraction algorithm adheres to two fundamental principles: (1) topographic consistency, assuming that the H-A relationship below the base water surface in the DEM is consistent with that derived from the nearshore slope [82]; (2) hydraulic connectivity, where topographic features constrain the expansion of the inundated area as the water level incrementally rises in the DEM. It first defines the reservoir's initial water surface in FABDEM, then iteratively raises the water level. The initial water surface consists of the grid cells in the DEM immediately upstream of the dam that share the same elevation and are interconnected, as indicated by the blue area labeled "Base water surface" in Figure 4c. At each rising step, the algorithm identifies adjacent grid cells that match the current surface edge elevation, expanding the inundation area to all neighboring cells at or below that elevation, thereby generating the corresponding H-A pairs. A schematic is shown in Figure 4a, while the delineated reservoir slope inundation zones are

presented in Figure 4c. Figure 4b graphically shows the obtained H-A-V curves and their mathematical expression.

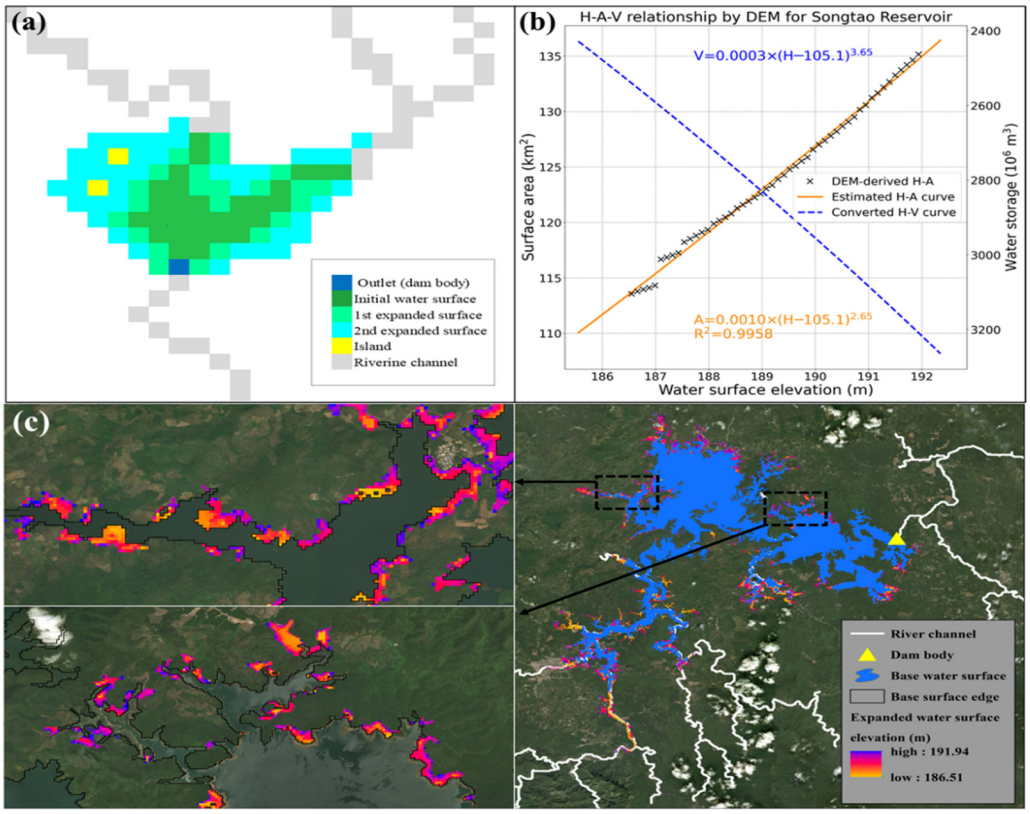

Figure 4. Water elevation-area-storage (*H-A-V*) relationship extraction method. (**a**) Schematic of the H-A extraction principle. (**b**) A three-parameter power function fits the *H-A* curve, which is converted to an *H-V* curve for storage estimation. (**c**) Visual validation of the extracted FABDEM's base water surface boundary (black line) and inundation slopes (colored) against the Landsat image (October 2018, ESRI).

Following the H-A pair extraction, the H-A curve was derived using a three-parameter power function. By integrating the H-A function (since surface area represents the derivative of storage volume), we derived the corresponding H-V relationship (Figure 4b). This conversion approach, detailed in Section S2, follows the methodology of Zhong, Zhao [40]. The resulting H-A-V relationships enable the derivation of volume time series (V) from observed water level (H) measurements.

3.3.2. Reconstructing Storage Dynamics

The original fused altimetry product for Songtao Reservoir [69], which contains large irregular temporal gaps, was interpolated to daily resolution using Piece wise Cubic Hermite Interpolation (PCHIP) [83]. Then, daily water storage variations were derived from daily altimetry using the H-V curve built in Section 3.3.1. A comparison between the reconstructed results and the ground truth is presented in Figure 5. The derived daily storage dynamics were subsequently applied to pre-calibrate the reservoir module parameters in the net section, serving as a viable substitute for ground observations.

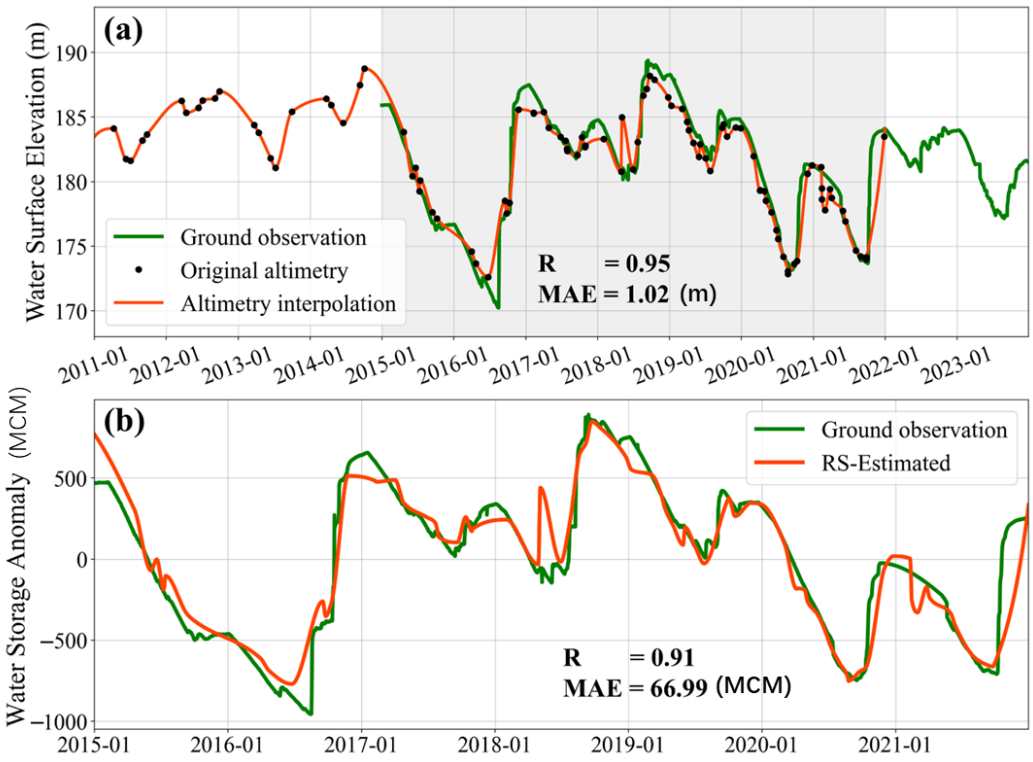

Figure 5. Validation of satellite-derived reservoir dynamics. (**a**) Daily water levels interpolated from fused satellite altimetry, compared to in situ observations. The gray area marks the overlapping period. (**b**) Remote sensing-derived storage anomalies (orange line, converted from altimetry data using the *H-A-V* curve) compared to ground observations (green line).

3.4. DRIVE-Dam Calibration and Experimental Setup

To evaluate the impact of the reservoir representation on model calibration performance, we conducted two single-site calibration experiments using the DRIVE-Dam model: CWD (with the reservoir module enabled) and CWOD (with the module disabled). CWOD is a conventional and widely used calibration configuration in which a purely natural-process hydrological model is calibrated even when the gauge is located downstream of a dam-regulated flow. By contrast, CWD explicitly simulates upstream reservoir behavior during calibration. Six parameters of the VIC (Table 2) were calibrated against observed flow from the Longtang station. The detailed meanings of each parameter are described in Section S3. Specifically, in the CWD, both the VIC's and the reservoir scheme's parameters (V_f, V_n, V_d, Q_n, Q_f, and k) needed to be determined, and simultaneous calibration would increase the complexity. Therefore, we designed a two-phase calibration strategy in CWD. In the first phase, the reservoir scheme was independently pre-calibrated against satellite-derived daily storage data, with the calibration and validation periods being 2011–2015 and 2016–2021, respectively. The inflow series from the CWOD results forced the pre-calibration. In the second phase, we fixed the reservoir parameters within the model and then optimized the VIC parameters. Note that, under this design, the reservoir dynamics from the pre-calibration result would inevitably differ from the final reservoir behavior simulated in CWD, because in the second phase, the inflow time series would be rescaled as the VIC parameter set varies. We present this acceptable discrepancy in Figure 6.

Table 2. Parameter calibration settings for VIC in the DRIVE-Dam.

Parameter	Unit	Calibration Range	Default Value in Baseline	Description
B_{infilt}	N/A	0.01–1.0	0.2	Variable infiltration curve parameter
D_s	fraction	0.01–1.0	1	Nonlinear baseflow onset proportion
Ds_{max}	mm/day	0.01–50.0	10	Maximum baseflow rate
W_s	fraction	0.01–1.0	0.65	Nonlinear baseflow threshold
d_2	m	0.30–2.0	1.5	Second soil layer thickness
d_3	m	0.30–2.0	1.5	Third soil layer thickness

Note: N/A, not applicable.

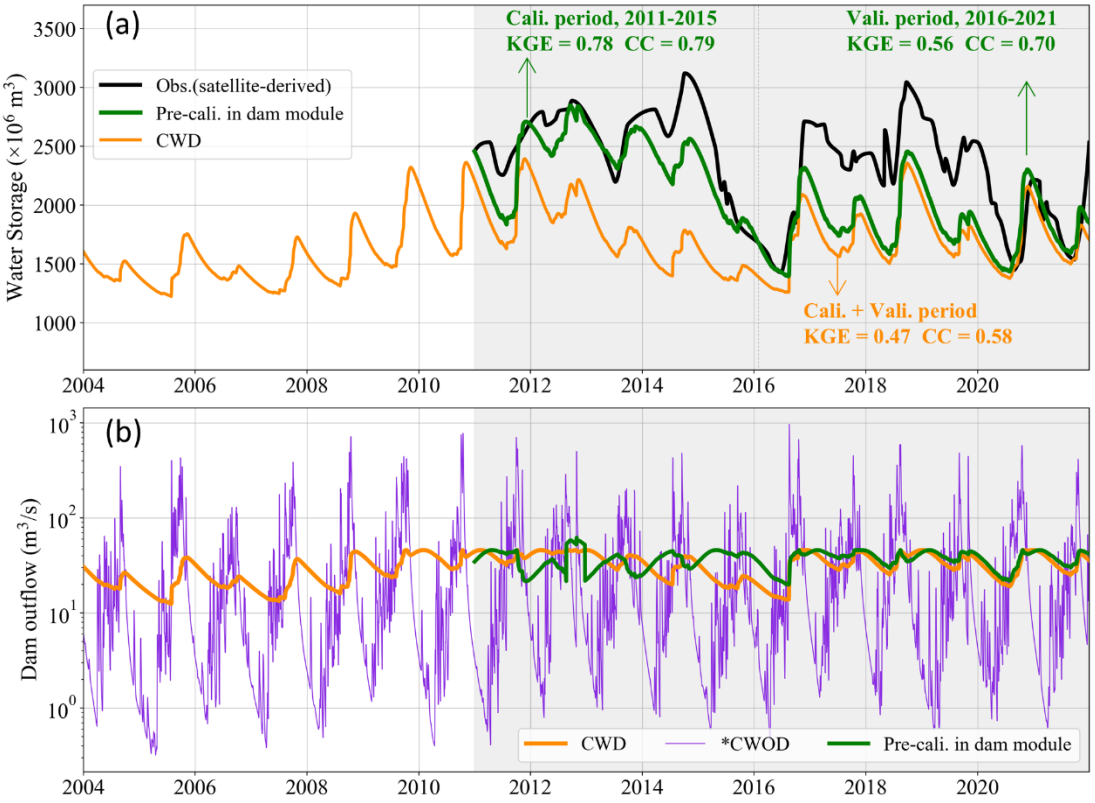

Figure 6. Validation of reservoir dynamics simulation: Pre-calibration vs. DRIVE-Dam calibration. (**a**) Water storage comparison: Pre-calibration (2011–2015) of the standalone dam module was performed against satellite-derived storage, forcing by inflow results from the CWOD. The optimized reservoir parameters from pre-calibration were then implemented in CWD. (**b**) Streamflow comparison at the dam location. For pre-calibration and CWD, the hydrographs show the dam release, whereas *CWOD denotes the natural flow. The grey area denotes the period used for pre-calibration and validation of the reservoir module.

All calibrations used the Kling-Gupta Efficiency (KGE) as the objective function. The dam module pre-calibration was performed using Particle Swarm Optimization (PSO) [84], while the VIC optimizations in CWD and CWOD were conducted with the Shuffled Complex Evolution-University of Arizona (SCE-UA) [85] algorithm. The DRIVE-Dam warm-up period was from 2001 to 2003, followed by a calibration and validation period of 2004–2010 and 2011–2017, respectively.

3.5. Performance Metrics and Model Evaluation

The evaluations were systematically performed on three aspects: (1) the reconstructed reservoir dynamics (Section 4.1), (2) the pre-calibration results of the dam module (Section 4.2), and (3) the flow modeling performance on three gauges under CWD and

CWOD (Sections 4.3 and 4.4). The selected long-term skill metrics include the Nash-Sutcliffe Efficiency (NSE), Kling-Gupta Efficiency (KGE), correlation coefficient (CC), percent bias (PBIAS), root mean square error (RMSE), and mean absolute error (MAE), which collectively quantify the agreement between simulated and observed data from multiple perspectives. Notably, model evaluation was conducted at three gauges rather than restricted to the calibration site (Longtang) to enable a more in-depth assessment of differences in the model's representation of basin-internal processes. Flood events were extracted from both simulated and observed flows to evaluate the flood capture ability using the probability of detection (POD), false alarm ratio (FAR), and critical success index (CSI). The flood identification threshold is defined as the 95th percentile of streamflow time series augmented by half a standard deviation, following the methodology established by Wu, Adler [17] for incorporating minor flood events. A flood event is defined when a day or any consecutive days exceed this threshold, while an exceeding day after a non-exceeding day marks the beginning of a new event. Thus, the flood duration of an event is the sum of its occurrence days. To evaluate the reproduction of flood event magnitudes, the relative peak flow error was assessed. Finally, analyses of runoff and baseflow responses during rainfall events in both the dry and wet seasons were conducted to diagnose the mechanisms underlying the differences between CWD and CWOD. All metrics were calculated as detailed in Section S4.

4. Results

4.1. Validation of Satellite-Derived Reservoir Dynamics

Figure 5 compares the reconstructed daily reservoir dynamics with the ground truth. Figure 5a shows that the interpolated high-frequency water levels smoothly connect the sparse altimetry points and match the observations. From 2015 to 2021, the CC is 0.95, with a MAE of 1.02 m. Some minor, explainable deviations exist; e.g., peaks and troughs in July 2016 and January 2018 were missed due to insufficient temporal coverage in the original altimetry data.

Figure 5b validates the storage anomalies derived by applying the H-V relationship (Section 3.3.1) to interpolated altimetry. The results correlate well with observations (CC = 0.91, slightly lower than for water levels), with a MAE of 66.99×10^6 m^3 (only ~2% of the reservoir's total capacity). Note that this robust fitness stems from direct interpolation of non-uniform and sparse multi-source altimetry data (104 points) to a long-term (4018 days) daily record. The result represents an improvement over the proposed approach from Dong, Yang [47], which relied on linear interpolation of single-frequency (10-day) altimetry products followed by rolling-mean smoothing to obtain daily estimates. The results highlight the flexibility of our approach and demonstrate the feasibility of using low-temporal-frequency satellite data for high-temporal-frequency hydrological modeling. The value of high-quality DEMs for reservoir dynamics reconstruction is also highlighted.

4.2. Pre-Calibration of Reservoir Operation Scheme

As depicted in Figure 6a, the pre-calibrated reservoir module successfully reproduced storage patterns during both the calibration (KGE = 0.78) and validation (KGE = 0.56) periods, demonstrating its robustness. Although the CWD result showed degraded storage simulation skills compared to the pre-calibration due to the fixed reservoir parameters and scaled inflow modeling by DRIVE, it derives good model efficiency with a KGE of 0.47 and a CC of 0.58. Figure 6b compares outflow results. The flow magnitudes from both the pre-calibration and CWD were comparable, substantially attenuating flood peaks while increasing dry-season flows relative to the naturally modeled flow (CWOD). This indicates the dam module's ability to perform critical reservoir functions, and the DRIVE-Dam model can represent reservoir dynamics.

4.3. Performance Evaluation of Streamflow Simulation

4.3.1. Long-Term Modeling Skills

Since this study focuses on an application scenario where only downstream hydrological observations are available for calibration, model performance is evaluated separately for the calibration and validation periods at the calibrated Longtang station. As shown in Table 3, the model demonstrates comparable simulation capabilities regardless of whether reservoirs are incorporated. Although NSE, KGE, and CC values are slightly lower during the validation period, they remain above 0.7, indicating that both calibration strategies ensure the model's hydrological applicability in this basin.

Table 3. Streamflow performance during the calibration and validation periods at the calibrated Longtang station.

Simulation Scenario	NSE		KGE		CC		PBIAS		RMSE	
	Cali.	Vali.	Cali.	Vali.	Cali.	Vali.	Cali.	Vali.	Cali.	Vali.
Baseline	0.53	0.49	0.45	0.39	0.79	0.76	−1.41	3.84	276.63	240.11
CWOD	0.84	0.72	0.83	0.77	0.93	0.86	12.92	11.99	160.56	175.88
CWD	0.84	0.78	0.87	0.76	0.92	0.88	7.96	9.41	162.90	157.69

Although the conventional CWOD strategy can effectively calibrate the model, its simulation skill within the basin is limited by the neglect of reservoir processes. This is substantiated by Figure 7, which extends the comparison from the downstream station to inner-basin stations. The superior performance of the CWD strategy is demonstrated by all skill metrics at each station. Notably, the significant improvement of CWD occurs at the Santan station (located at the tributary, unaffected by dam regulation), with NSE, KGE, and CC increasing by 0.10, 0.08, and 0.06, respectively. The improved parameterization from explicit reservoir representation boosts model accuracy across both reservoir-influenced and uninfluenced regions. The simulated long-term flow hydrographs are provided in Section S5.

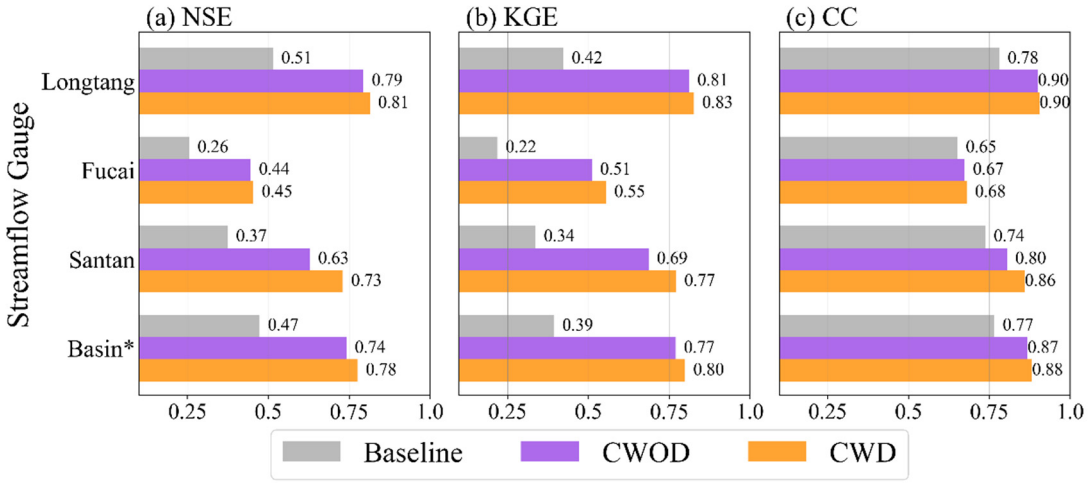

Figure 7. Comparison of long-term flow performance metrics under two calibration scenarios at each station and the basin scale, covering 2004–2017. (**a**) Nash-Sutcliffe Efficiency (NSE), (**b**) Kling-Gupta Efficiency (KGE), and (**c**) Correlation Coefficient (CC). *Basin** denotes a weighted aggregation of the three hydrological stations based on their average streamflow.

4.3.2. Flow Duration and Seasonality

The flow duration curves (Figure 8a–c) revealed nuanced differences between CWD and CWOD in simulating flows across various magnitudes. Under low-to-moderate flow

conditions (≥50% exceedance probability), CWOD consistently underestimated flows, whereas CWD more closely aligned with observed flows. This indicated that reservoir-aided parameterization improved dry-season flow estimations across watersheds (see hydrographs in Section S5). For the high-flow regime (see inset panels), CWD generated higher simulated extreme flows (top 1%) than CWOD at all stations, showing better agreement with observations. Conversely, within the 1–6% exceedance range, an inverse contrast is observed, attributed to the tendency of CWOD-optimized parameters to overestimate flood tails.

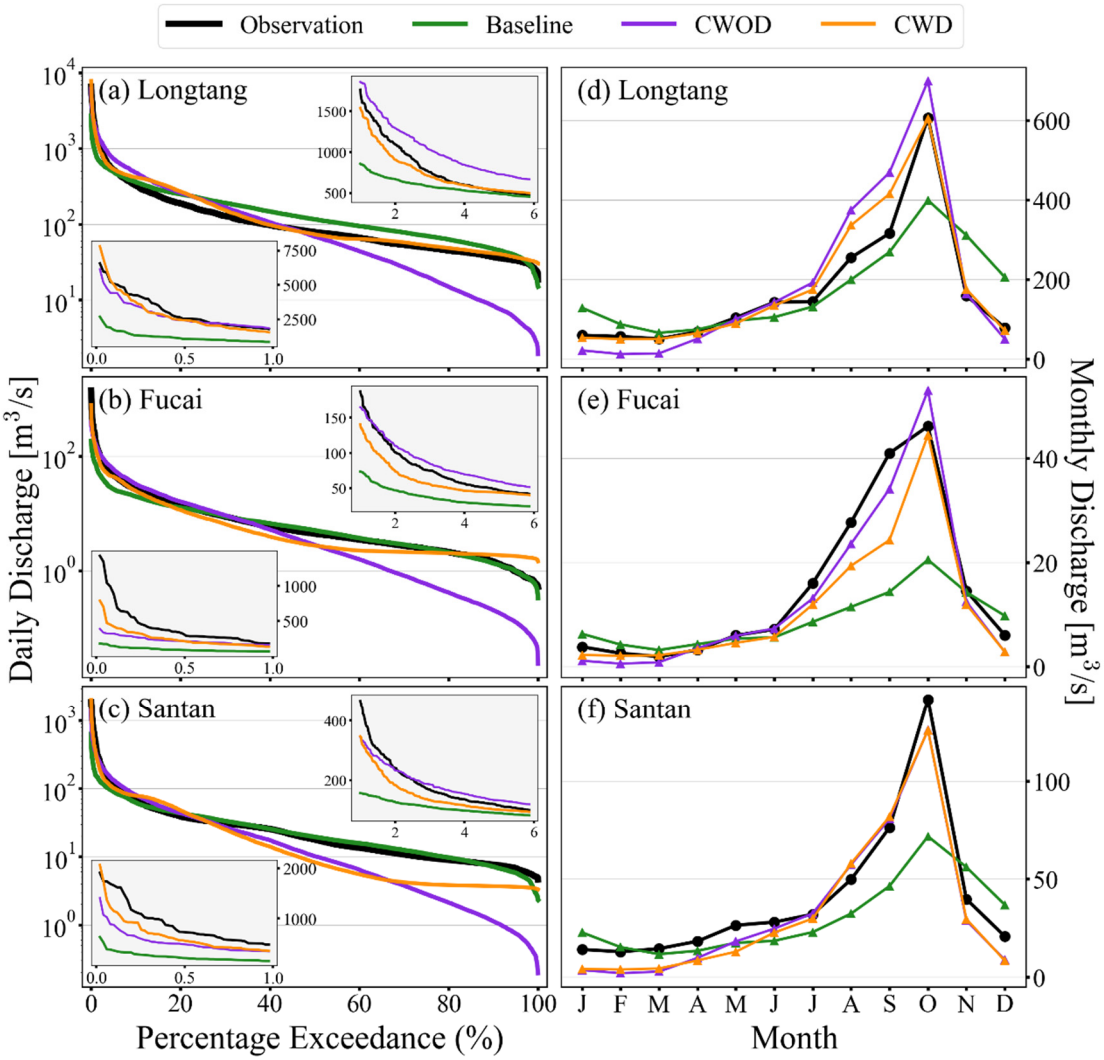

Figure 8. Evaluation of flow duration and seasonality. (**a**–**c**) Flow Duration Curves at each station, showing ranked daily flow comparisons over the entire run period (2004–2017), reflecting model performance across different flow magnitudes. Dual insets within each panel highlight detailed representations of high flow (with 0–1 and 1–6 percentage exceedance, respectively). (**d**–**f**) Seasonal variations.

Streamflow seasonality analysis (Figure 8d–f) demonstrated that CWD better captured the reservoir's regulatory effects at the Longtang station, as evidenced by higher dry-season flows and lower wet-season flows. This is attributed to the fact that during the flood season, the reservoir's primary functions are flood-peak attenuation and impoundment of upstream inflows, resulting in average flows below the natural regime. Conversely, during the dry season, the reservoir releases stored water to support downstream irrigation and domestic demands, leading to average flows exceeding natural conditions. In contrast, CWOD, constrained by the model's natural process structure, exaggerated seasonal variations,

indicating that CWD is a preferable approach for reproducing intra-annual streamflow distribution patterns.

4.4. Model Skills in Capturing Flood Events

4.4.1. Flood Event Detection Capability

Figure 9 demonstrates that CWD outperforms CWOD in detecting flood events. In the basin-wide event evaluation, compared to CWOD, CWD increased the POD by 0.06, reduced the FAR by 0.13, and improved the CSI by 0.09. Importantly, DRIVE-Dam significantly reduced FAR and addressed the issue reported by Wu, Adler [17] that hydrological models without explicit reservoir-dam simulation tend to derive high FAR. Reducing false alarms is critical to avoid ineffective efforts in flood warning and response. As shown in Figure 9, the most significant reduction in FAR (from 0.33 to 0.12) was achieved at Fucai Station, indicating that reservoir-induced better parameterization improves upstream hydrological simulation. This is a positive outcome, as headwater regions are often prone to flash floods but remain challenging for DHMs to simulate accurately.

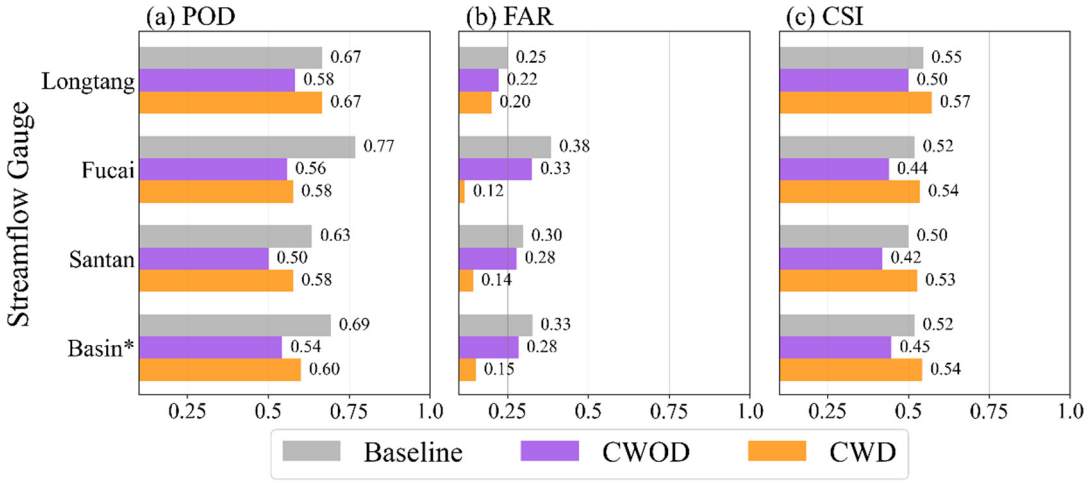

Figure 9. Evaluation of flood event detection capability: (**a**) Probability of Detection (POD), (**b**) False Alarm Ratio (FAR), and (**c**) Critical Success Index (CSI). The *Basin** represents the aggregated flood events from all stations.

Additionally, the baseline model outperformed CWOD in terms of POD and CSI, suggesting that even without calibration, the model can effectively detect the occurrence of flood events, relying on relative (rather than absolute) values and statistical metrics derived from the long-term simulations. However, the CWD demonstrated better overall performance than the baseline on the CSI metric, attributable to significant improvements in both magnitude (indicated by NSE and KGE scores) and timing (indicated by the CC score), as illustrated in Figure 7.

4.4.2. Flood Peak and Duration

Further evaluation of the flood events shows that the CWD yielded more accurate flood peaks than CWOD, as illustrated in Figure 10a. Compared to the baseline model, both calibration strategies significantly improve the realism of peak flow. However, CWD exhibits a consistently narrower error distribution than CWOD, indicating greater stability and consistency, with reduced variability in peak flow errors across events. At the Longtang and Santan stations, the median and mean errors under CWD are closer to zero, indicating lower systematic bias. Furthermore, uncertainty in peak flow errors decreases with increasing catchment area (Fucai < Santan < Longtang). Notably, at the calibrated Longtang station, the exceptionally low errors achieved by the CWD can be attributed to

two factors: the use of optimized model parameters and the activation of the reservoir module, which captures the human regulation effect—specifically, the upstream dam's attenuation of flood peaks being effectively transmitted to the downstream gauge.

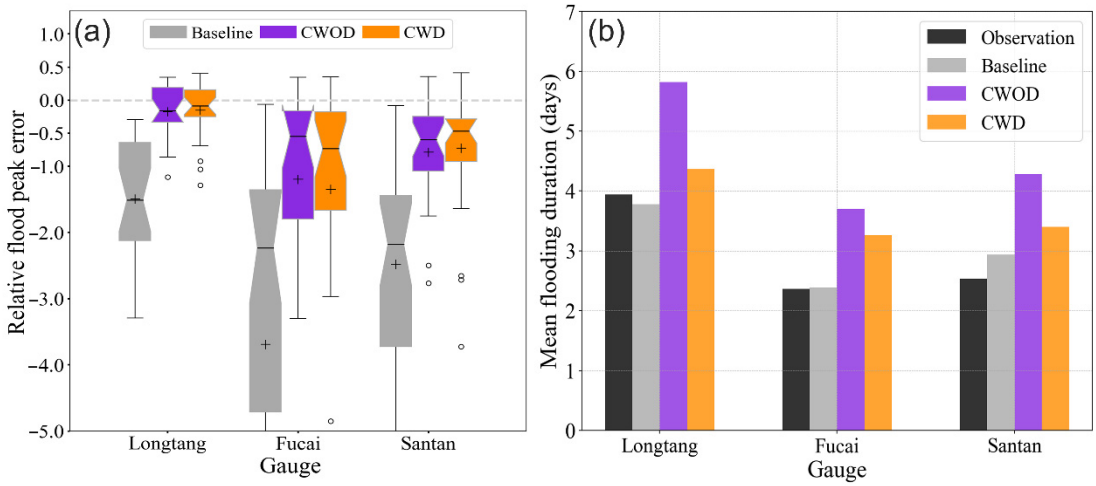

Figure 10. Comparison of flood peak flow and duration. (**a**) Boxplots of relative peak flow error (on hit events). (**b**) Bar plots comparing simulated and observed mean flooding duration.

Regarding flood event duration, the CWOD exhibits a larger bias than CWD, consistently overestimating flooded time across all stations (Figure 10b). At the two interior hydrologic gauges, the overestimation stems from flawed parameters generated by CWOD, which is led by a relatively flattened hydrograph (see Section 5.2 for details). The two-day overestimation of mean event duration at the downstream Longtang Station reflects both parameterization deficiencies and omitted reservoir operations. In summary, CWD outperforms CWOD in flood event detection, peak flow error, and event duration, while also improving simulation accuracy at both calibrated and inner-basin sites. Thus, CWD is the recommended calibration strategy for flood prediction.

5. Discussion

5.1. Advanced H-A-V Extraction Based on Water Connectivity

The consistent precision of the reconstructed water levels and storage anomalies (Section 4.1) implies that the developed H-A-V curve extraction algorithm, coupled with FABDEM, reliably characterizes the water storage-elevation relationship. The novelty of the algorithm lies in its effective use of both hydrological connectivity and terrain-slope constraints on water expansion. Conventional curve-extraction algorithms typically delineate the maximum reservoir area and then statistically aggregate the water surface area at different elevation levels within this boundary [50,52,86], thereby inherently ignoring hydrological connectivity along the water-land boundary and potentially leading to overestimation of water surface area.

We specifically evaluate the accuracy of reconstructed storage anomalies rather than absolute values because the outflow calculation (Equations (1) and (2)) relies on water volume changes rather than absolute storage. In other words, satellite-derived water storage dynamics—even when absolute values are over- or underestimated due to unknown subaqueous topography in DEMs—remain valid for calibrating and validating operational schemes as long as their relative variations are precise. This is critical for reservoir modeling practitioners. We tested three publicly available reservoir bathymetry datasets [87–89] for 13 reservoirs across Hainan Island, mainland China, and eastern Africa. We found that the provided H-A-V curves were unsuitable for water balance calculations. This limitation

likely stems from these curves' focus on approximating complete underwater bathymetry, which compromises their accuracy within the actual range of water-level fluctuations in the active storage room [90]. Therefore, we suggest that in outflow-oriented reservoir modeling, accurate relative variations are sufficient when bathymetry/storage data are inaccessible.

5.2. Diagnosis of Hydrological Response Mechanism

To elucidate the mechanistic differences between calibration strategies, we conducted two diagnostic analyses on a wet-season heavy rainfall event (Figure 11) and a dry-season minor event (Figure 12). Comparative assessment of hydrological responses reveals that: (1) During wet conditions (Figure 11d–f), CWOD generates exaggerated baseflow but attenuated runoff, resulting in underestimated flood peaks with prolonged recession (Figure 11a–c), whereas CWD better matches observed flood pulses; (2) Under dry conditions, CWD generates lower runoff and higher baseflow than CWOD (Figure 12d–f), leading to sustained higher streamflow (Figure 12a–c). The discrepancies originate from the distinct characteristics of the two calibrated VIC parameter sets (Table 4). The relationship between parameter values and hydrological responses is provided in Section S3.

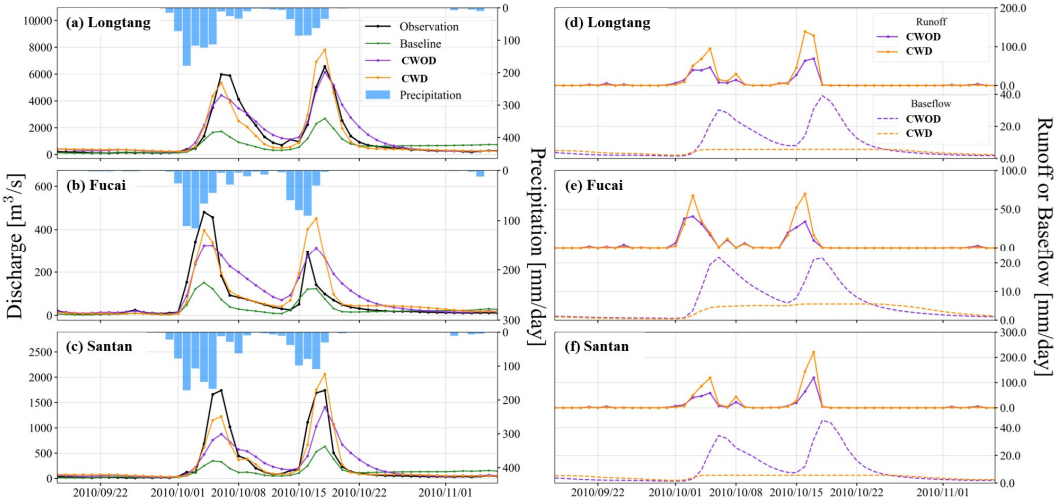

Figure 11. Hydrological response to an extreme rainfall event in the wet season. (**a**–**c**) Simulated vs. observed flows at three stations. (**d**–**f**) Time series of VIC-derived surface runoff and baseflow under different calibration strategies.

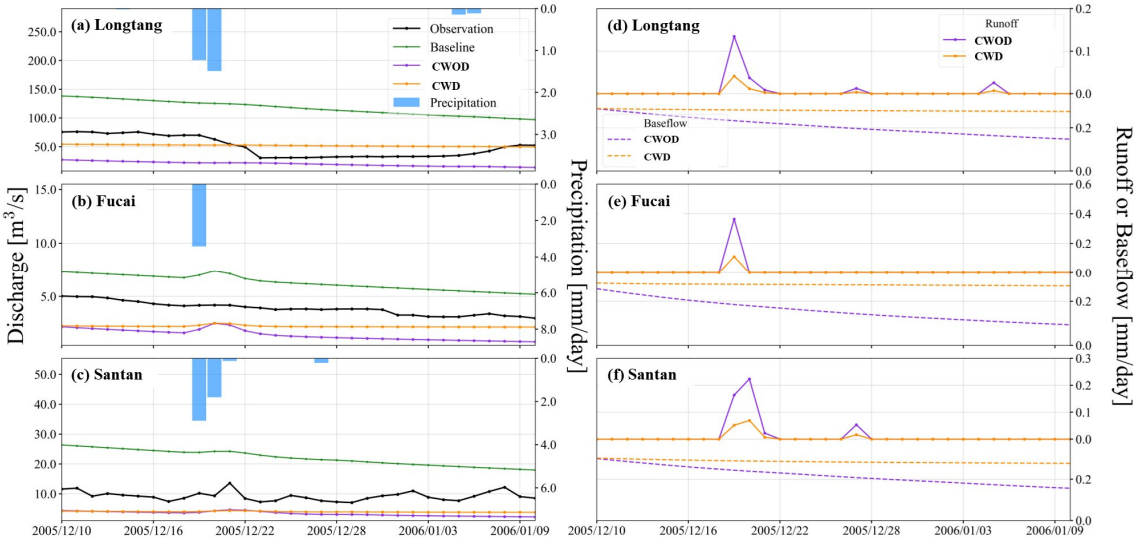

Figure 12. Same as Figure 11, but for a minor rainfall event during the dry season.

Table 4. Calibrated parameter values of the VIC model in the DRIVE-Dam.

Scenario	Parameter					
	B_{infilt}	D_s	Ds_{max}	W_s	d_2	d_3
CWOD	0.44	0.43	31.80	0.11	1.49	0.54
CWD	0.12	0.05	5.65	0.95	0.69	1.35

The underlying reasons for the above phenomena are as follows. During calibration in the CWOD, due to the natural physical structure, unregulated flood flows from the model are adjusted to match the dam-attenuated flood-peak observations. This mismatch compels the model to reproduce dampened hydrological responses under extreme rainfall, typically manifested as elevated baseflow and suppressed runoff. This may also explain the significant reduction in POD by CWOD compared to the uncalibrated baseline simulations. At the same time, CWD led to more balanced POD and FAR pairs through more reasonable process delineation and parameterization. This response style is propagated across the basin by the lumped parameter setting. In contrast, during the dry season, CWD enables parameter optimization to account for reservoir-induced supplemental water relative to natural flows, leading to higher streamflow estimates than CWOD. These findings support our motivated hypothesis: The absence of reservoir representation in the CWOD distorts the parameters, proving that physical structure completeness benefits parameterization. Figure 13 further illustrates these spatial discrepancies by visualizing flow patterns during specific event days, thereby elucidating the divergent hydrological responses between CWD and CWOD, particularly within headwater regions.

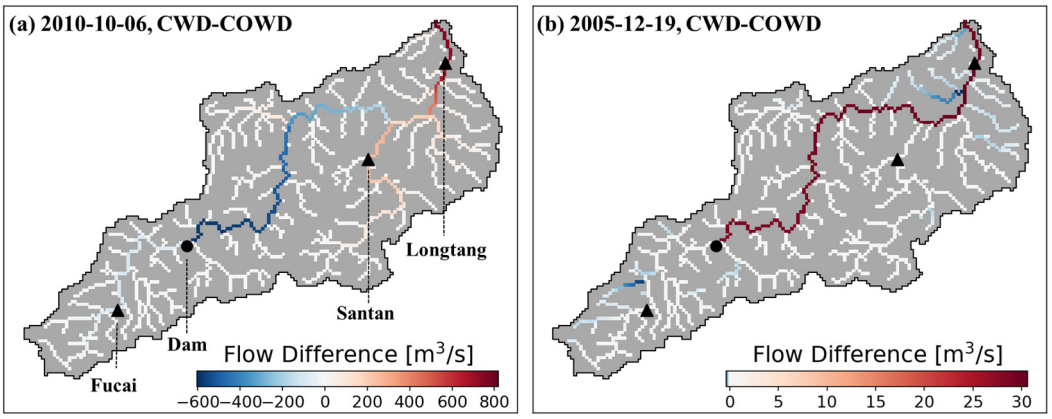

Figure 13. Spatial differences in streamflow between CWD and CWOD during two rainfall events. (**a**) A wet season extreme event occurred on 6 October 2010. (**b**) A minor rainfall event during the dry season.

These findings highlight the critical need to account for watershed-scale effectiveness when calibrating models. CWOD is an effective strategy for the calibrated station (NSE = 0.79, KGE = 0.81) even when reservoirs exist upstream, as the lumped parameters inherently integrate and dampen intra-watershed noise. However, its effectiveness is confined to the calibrated site, achieved at the expense of flow fidelity in upstream areas. CWD spatially enhances model efficacy across the basin. For instance, at the Santan station (unaffected by the dam), NSE and KGE increased by 0.10 and 0.08, respectively, compared to CWOD, while the FAR decreased by 0.14. Such improvements are critical for flood forecasting, as human settlements are often distributed along diverse river reaches. Recent research [91] provides evidence that global headwater streamflow is increasing, elevating

extreme flood risks—a pressing concern. The CWD strategy should be prioritized for such regions.

5.3. Synergistic Benefits of Enhanced Model Structure and Parameterization

The CWD results underscore that the integrity of the model's physical structure is a prerequisite for accurate parameterization, as evidenced by the physically sound parameters led by the reservoir scheme's integration into the DRIVE. Although our experiments were conducted under lumped SSC—a classical hydrological scenario, the proposed methodology holds inherent extensibility. Alternative calibration approaches (e.g., cascade-sequential calibration or multi-site calibration) essentially constitute spatial extensions of this fundamental structure, in which a dam upstream of a gauge represents a localized SSC scenario. The CWD enables the model to reproduce reasonable natural hydrological processes in dammed watersheds, serving as a viable alternative to conventional parameter regionalization methods and expanding the model's applicability for scientific research. Thus, we advocate for a paradigm shift in hydrological modeling from traditional calibration approaches to the CWD strategy.

6. Conclusions

This study proposes a comprehensive DHM calibration framework to address the misrepresentation of basin-internal hydrological processes in dammed watersheds, thereby enhancing the model realism. The framework integrates a satellite-based reservoir module into DHM and explicitly incorporates the reservoir storage–release processes into parameter calibration. In the case study, long-term reservoir dynamics—including water level and storage—were reconstructed by integrating satellite altimetry with DEM-derived topographic data. The reconstructed dynamics were subsequently utilized to establish and pre-calibrate the reservoir operation scheme embedded within the coupled DRIVE-Dam model. Finally, the DRIVE-Dam was calibrated against observed streamflow near the basin outlet. Specifically, we assessed how integrating the reservoir process into the calibration influences the representation of hydrological variables across the basin. The key findings are as follows:

1. High-temporal-resolution (daily) reservoir dynamics can be successfully reconstructed by combining sparse satellite altimetry with DEM-derived topographic information, supporting the development of reservoir operation schemes under data-scarce conditions.
2. The explicit representation of reservoir processes contributes positively to DHM parameter optimization, improving the rainfall-runoff responsive behavior across the watershed. In particular, flood modeling performance was notably enhanced, with the POD increasing from 0.54 to 0.60 and the FAR decreasing from 0.28 to 0.15. The improvements originate from the calibration process, with the simulated hydrograph reflecting dam-induced flood peak attenuation in wet seasons and water supplementation in dry seasons, closely matching downstream regulated observations.
3. Although the conventional dam-excluded calibration achieves acceptable performance at the basin outlet, it compromises accuracy in upstream regions. The loss of accuracy is manifested in the flood hydrograph shapes, which are characterized by subdued flood impulses and prolonged flood recession. The deterioration stems from spurious parameters arising from calibrating a reservoir-free model (simulating natural flow) against dam-regulated observations, leading to an unreasonable partitioning of baseflow versus surface runoff.

The findings highlight the benefits of accounting for anthropogenic activities in model calibration. The results underscore the significant potential of satellite data to advance

hydrological modeling. With the increasing spatial and temporal coverage of Earth observations, such as the Surface Water and Ocean Topography (SWOT) mission [92], this research is expected to offer methodological reference for flood monitoring and early warning in human-impacted regions.

Supplementary Materials: The following supporting information can be downloaded at: https://www.mdpi.com/article/10.3390/rs18020193/s1, Section S1: Detailed Description of Reservoir Module; Section S2: H-A-V Relationship Equations; Section S3: The Meaning of the Six Calibrated Parameters in the VIC Model; Section S4: Skill Metrics for Evaluating Estimation; Section S5: Hydrographs of Three Stations; Figure S1: Relationship between multiplier r (r_1 or r_2) and reservoir storage filling ratio under different k values in the operation scheme. For Songtao Reservoir in this study, k was calibrated as 0.6; Figure S2: Comparison of daily storage simulation skill for reservoir schemes across 11 reservoirs in mainland China—DRIVE-Dam Scheme vs. LISFLOOD Scheme. Calibration period: 2019–2020; Validation period: 2020–2021; Figure S3: Streamflow time series of Longtang Station. (a) Calibration period. (b) Validation period; Figure S4: Streamflow time series of Fucai Station. (a) 2004–2010; (b) 2011–2017. Note that this station serves as an auxiliary validation site and was not involved in the parameter calibration of the DRIVE-Dam model; Figure S5: Same as Figure S4, but for Santan Station; Table S1: Module Parameter Settings for Songtao Reservoir; Table S2: Information on the 11 tested reservoirs in Figure S2; Table S3: Skill Metrics for Evaluating Estimation.

Author Contributions: C.L.: Writing—original manuscript, conceptualization, formal analysis, investigation, methodology development, software development, validation, data collection and analyses, visualization of results. H.W.: Writing—review & editing, supervision. L.A.: Writing—review & editing. Y.M.: Writing—review & editing. N.N.: Writing—review & editing. Z.H.: Data Curation. Y.H.: Data Curation. L.Q.: Data Curation. All authors have read and agreed to the published version of the manuscript.

Funding: This study was supported by the National Natural Science Foundation of China (Grants 42275019 and 42088101), the National Key R&D Program of China (Grant 2024YFC3013302), and the Open Fund Project for Heavy Rain of China Meteorological Administration (Grant BYKJ2024Z10). Partial support was also provided by the Hainan Provincial R&D Program (Grants CXFZ2022J074 and SCSF202203), the Hainan Key Research and Development Project (Grant ZDYF2023SHFZ125), and the International Program Fund for Young Scientific Research Talents in Guangdong Provincial Colleges and Universities.

Data Availability Statement: The altimetry data of Songtao Reservoir are openly available at https://zenodo.org/records/7251283 (accessed on 30 December 2025). The FABDEM data are openly available from the University of Bristol (https://data.bris.ac.uk/data/dataset/s5hqmjcdj8yo2ibzi9b4ew3sn (accessed on 30 December 2025)). The observed reservoir water level and storage data were collected from the Large Reservoir Hydrological Information Website of the Ministry of Water Resources of China (http://xxfb.mwr.cn/sq_dxsk.html, accessed on 30 December 2025). Streamflow observations from three hydrological stations in the Nandu River Basin were obtained from the Hainan Provincial Meteorological Bureau and are available on request from the corresponding author with the permission of the bureau.

Conflicts of Interest: The authors declare no conflict of interest.

References

1. Duan, Z.; Bastiaanssen, W.G.M. Estimating water volume variations in lakes and reservoirs from four operational satellite altimetry databases and satellite imagery data. *Remote Sens. Environ.* **2013**, *134*, 403–416. [CrossRef]
2. Chao, B.F.; Wu, Y.H.; Li, Y.S. Impact of Artificial Reservoir Water Impoundment on Global Sea Level. *Science* **2008**, *320*, 212–214. [CrossRef]
3. Spinti, R.A.; Condon, L.E.; Zhang, J. The evolution of dam induced river fragmentation in the United States. *Nat. Commun.* **2023**, *14*, 3820. [CrossRef]

4. Belletti, B.; Garcia de Leaniz, C.; Jones, J.; Bizzi, S.; Borger, L.; Segura, G.; Castelletti, A.; van de Bund, W.; Aarestrup, K.; Barry, J.; et al. More than one million barriers fragment Europe's rivers. *Nature* **2020**, *588*, 436–441. [CrossRef]
5. Grill, G.; Lehner, B.; Thieme, M.; Geenen, B.; Tickner, D.; Antonelli, F.; Babu, S.; Borrelli, P.; Cheng, L.; Crochetiere, H.; et al. Mapping the world's free-flowing rivers. *Nature* **2019**, *569*, 215–221. [CrossRef]
6. Haddeland, I.; Heinke, J.; Biemans, H.; Eisner, S.; Flörke, M.; Hanasaki, N.; Konzmann, M.; Ludwig, F.; Masaki, Y.; Schewe, J.; et al. Global water resources affected by human interventions and climate change. *Proc. Natl. Acad. Sci. USA* **2014**, *111*, 3251–3256. [CrossRef] [PubMed]
7. Lettenmaier, D.P.; Milly, P.C.D. Land waters and sea level. *Nat. Geosci.* **2009**, *2*, 452–454. [CrossRef]
8. Hanasaki, N.; Kanae, S.; Oki, T. A reservoir operation scheme for global river routing models. *J. Hydrol.* **2006**, *327*, 22–41. [CrossRef]
9. Zhao, F.; Veldkamp, T.I.E.; Frieler, K.; Schewe, J.; Ostberg, S.; Willner, S.; Schauberger, B.; Gosling, S.N.; Schmied, H.M.; Portmann, F.T.; et al. The critical role of the routing scheme in simulating peak river discharge in global hydrological models. *Environ. Res. Lett.* **2017**, *12*, 075003. [CrossRef]
10. Poff, N.L.; Allan, J.D.; Bain, M.B.; Karr, J.R.; Prestegaard, K.L.; Richter, B.D.; Sparks, R.E.; Stromberg, J.C. The Natural Flow Regime. *BioScience* **1997**, *47*, 769–784. [CrossRef]
11. Wang, W.; Li, H.Y.; Leung, L.R.; Yigzaw, W.; Zhao, J.S.; Lu, H.; Deng, Z.Q.; Demisie, Y.; Blöschl, G. Nonlinear Filtering Effects of Reservoirs on Flood Frequency Curves at the Regional Scale. *Water Resour. Res.* **2017**, *53*, 8277–8292. [CrossRef]
12. Arias, M.E.; Cochrane, T.A.; Kummu, M.; Lauri, H.; Holtgrieve, G.W.; Koponen, J.; Piman, T. Impacts of hydropower and climate change on drivers of ecological productivity of Southeast Asia's most important wetland. *Ecol. Model.* **2014**, *272*, 252–263. [CrossRef]
13. Tsai, W.P.; Feng, D.; Pan, M.; Beck, H.; Lawson, K.; Yang, Y.; Liu, J.; Shen, C. From calibration to parameter learning: Harnessing the scaling effects of big data in geoscientific modeling. *Nat. Commun.* **2021**, *12*, 5988. [CrossRef]
14. Chlumsky, R.; Mai, J.; Craig, J.R.; Tolson, B.A. Simultaneous Calibration of Hydrologic Model Structure and Parameters Using a Blended Model. *Water Resour. Res.* **2021**, *57*, e2020WR029229. [CrossRef]
15. Kupzig, J.; Kupzig, N.; Floerke, M. Regionalization in global hydrological models and its impact on runoff simulations: A case study using WaterGAP3 (v 1.0.0). *Geosci. Model Dev.* **2024**, *17*, 6819–6846. [CrossRef]
16. Gupta, H.V.; Sorooshian, S.; Yapo, P.O. Toward improved calibration of hydrologic models: Multiple and noncommensurable measures of information. *Water Resour. Res.* **1998**, *34*, 751–763. [CrossRef]
17. Wu, H.; Adler, R.F.; Tian, Y.; Huffman, G.J.; Li, H.; Wang, J. Real-time global flood estimation using satellite-based precipitation and a coupled land surface and routing model. *Water Resour. Res.* **2014**, *50*, 2693–2717. [CrossRef]
18. Andersen, J.; Refsgaard, J.C.; Jensen, K.H. Distributed hydrological modelling of the Senegal River Basin-Model construction and validation. *J. Hydrol.* **2001**, *247*, 200–214. [CrossRef]
19. Ajami, N.K.; Gupta, H.; Wagener, T.; Sorooshian, S. Calibration of a semi-distributed hydrologic model for streamflow estimation along a river system. *J. Hydrol.* **2004**, *298*, 112–135. [CrossRef]
20. Arsenault, R.; Brissette, F.; Martel, J.L. The hazards of split-sample validation in hydrological model calibration. *J. Hydrol.* **2018**, *566*, 346–362. [CrossRef]
21. Duan, Q.; Sorooshian, S.; Gupta, V.K. Optimal use of the SCE-UA global optimization method for calibrating watershed models. *J. Hydrol.* **1994**, *158*, 265–284. [CrossRef]
22. Shen, H.; Tolson, B.A.; Mai, J. Time to Update the Split-Sample Approach in Hydrological Model Calibration. *Water Resour. Res.* **2022**, *58*, e2021WR031523. [CrossRef]
23. Sun, R.; Hernández, F.; Liang, X.; Yuan, H. A Calibration Framework for High-Resolution Hydrological Models Using a Multiresolution and Heterogeneous Strategy. *Water Resour. Res.* **2020**, *56*, e2019WR026541. [CrossRef]
24. Vansteenkiste, T.; Tavakoli, M.; Van Steenbergen, N.; De Smedt, F.; Batelaan, O.; Pereira, F.; Willems, P. Intercomparison of five lumped and distributed models for catchment runoff and extreme flow simulation. *J. Hydrol.* **2014**, *511*, 335–349. [CrossRef]
25. Smith, M.B.; Koren, V.; Zhang, Z.Y.; Zhang, Y.; Reed, S.M.; Cui, Z.T.; Moreda, F.; Cosgrove, B.A.; Mizukami, N.; Anderson, E.A.; et al. Results of the DMIP 2 Oklahoma experiments. *J. Hydrol.* **2012**, *418*, 17–48. [CrossRef]
26. Pokhrel, P.; Gupta, H.V. On the ability to infer spatial catchment variability using streamflow hydrographs. *Water Resour. Res.* **2011**, *47*, W08534. [CrossRef]
27. Alfieri, L.; Burek, P.; Dutra, E.; Krzeminski, B.; Muraro, D.; Thielen, J.; Pappenberger, F. GloFAS-global ensemble streamflow forecasting and flood early warning. *Hydrol. Earth Syst. Sci.* **2013**, *17*, 1161–1175. [CrossRef]
28. Alfieri, L.; Libertino, A.; Campo, L.; Dottori, F.; Gabellani, S.; Ghizzoni, T.; Masoero, A.; Rossi, L.; Rudari, R.; Testa, N.; et al. Impact-based flood forecasting in the Greater Horn of Africa. *Nat. Hazards Earth Syst. Sci.* **2024**, *24*, 199–224. [CrossRef]
29. Najafi, H.; Shrestha, P.K.; Rakovec, O.; Apel, H.; Vorogushyn, S.; Kumar, R.; Thober, S.; Merz, B.; Samaniego, L. High-resolution impact-based early warning system for riverine flooding. *Nat. Commun.* **2024**, *15*, 3726. [CrossRef]

30. Han, J.-C.; Huang, G.-H.; Zhang, H.; Li, Z.; Li, Y.-P. Effects of watershed subdivision level on semi-distributed hydrological simulations: Case study of the SLURP model applied to the Xiangxi River watershed, China. *Hydrol. Sci. J.* **2013**, *59*, 108–125. [CrossRef]
31. Dang, T.D.; Chowdhury, A.F.M.K.; Galelli, S. On the representation of water reservoir storage and operations in large-scale hydrological models: Implications on model parameterization and climate change impact assessments. *Hydrol. Earth Syst. Sci.* **2020**, *24*, 397–416. [CrossRef]
32. Alfieri, L.; Bucherie, A.; Libertino, A.; Campo, L.; D'Andrea, M.; Ghizzoni, T.; Gabellani, S.; Massabò, M.; Rossi, L.; Rudari, R.; et al. Operational impact-based flood early warning in Lao PDR and Cambodia. *Int. J. Disaster Risk Reduct.* **2025**, *128*, 105718. [CrossRef]
33. Gou, J.; Miao, C.; Duan, Q.; Tang, Q.; Di, Z.; Liao, W.; Wu, J.; Zhou, R. Sensitivity Analysis-Based Automatic Parameter Calibration of the VIC Model for Streamflow Simulations Over China. *Water Resour. Res.* **2020**, *56*, e2019WR025968. [CrossRef]
34. Gou, J.; Miao, C.; Samaniego, L.; Xiao, M.; Wu, J.; Guo, X. CNRD v1.0 a high-quality natural runoff dataset for hydrological and climate studies in China. *Bull. Am. Meteorol. Soc.* **2021**, *102*, E929–E947. [CrossRef]
35. Miao, C.; Gou, J.; Fu, B.; Tang, Q.; Duan, Q.; Chen, Z.; Lei, H.; Chen, J.; Guo, J.; Borthwick, A.G.L.; et al. High-quality reconstruction of China's natural streamflow. *Sci. Bull.* **2022**, *67*, 547–556. [CrossRef]
36. Beck, H.E.; van Dijk, A.I.J.M.; de Roo, A.; Miralles, D.G.; McVicar, T.R.; Schellekens, J.; Bruijnzeel, L.A. Global-scale regionalization of hydrologic model parameters. *Water Resour. Res.* **2016**, *52*, 3599–3622. [CrossRef]
37. Beck, H.E.; Pan, M.; Lin, P.; Seibert, J.; van Dijk, A.I.J.M.; Wood, E.F. Global Fully Distributed Parameter Regionalization Based on Observed Streamflow From 4,229 Headwater Catchments. *J. Geophys. Res. Atmos.* **2020**, *125*, e2019JD031485. [CrossRef]
38. Song, C.Q.; Fan, C.Y.; Zhu, J.Y.; Wang, J.D.; Sheng, Y.W.; Liu, K.; Chen, T.; Zhan, P.F.; Luo, S.X.; Yuan, C.Y.; et al. A comprehensive geospatial database of nearly 100 000 reservoirs in China. *Earth Syst. Sci. Data* **2022**, *14*, 4017–4034. [CrossRef]
39. Shrestha, P.K.; Samaniego, L.; Rakovec, O.; Kumar, R.; Mi, C.; Rinke, K.; Thober, S. Toward Improved Simulations of Disruptive Reservoirs in Global Hydrological Modeling. *Water Resour. Res.* **2024**, *60*, e2023WR035433. [CrossRef]
40. Zhong, R.; Zhao, T.; Chen, X. Hydrological Model Calibration for Dammed Basins Using Satellite Altimetry Information. *Water Resour. Res.* **2020**, *56*, e2020WR027442. [CrossRef]
41. Wu, Y.; Chen, J. An operation-based scheme for a multiyear and multipurpose reservoir to enhance macroscale hydrologic models. *J. Hydrometeorol.* **2012**, *13*, 270–283. [CrossRef]
42. Wang, K.; Shi, H.; Chen, J.; Li, T. An improved operation-based reservoir scheme integrated with Variable Infiltration Capacity model for multiyear and multipurpose reservoirs. *J. Hydrol.* **2019**, *571*, 365–375. [CrossRef]
43. Yassin, F.; Razavi, S.; Elshamy, M.; Davison, B.; Sapriza-Azuri, G.; Wheater, H. Representation and improved parameterization of reservoir operation in hydrological and land-surface models. *Hydrol. Earth Syst. Sci.* **2019**, *23*, 3735–3764. [CrossRef]
44. Speckhann, G.A.; Kreibich, H.; Merz, B. Inventory of dams in Germany. *Earth Syst. Sci. Data* **2021**, *13*, 731–740. [CrossRef]
45. Brunner, M.I.; Slater, L.; Tallaksen, L.M.; Clark, M. Challenges in modeling and predicting floods and droughts: A review. *Wiley Interdiscip. Rev.-Water* **2021**, *8*, e1520. [CrossRef]
46. Steyaert, J.C.; Condon, L.E.; Turner, S.W.D.; Voisin, N. ResOpsUS, a dataset of historical reservoir operations in the contiguous United States. *Sci. Data* **2022**, *9*, 34. [CrossRef]
47. Dong, N.; Yang, M.; Wei, J.; Arnault, J.; Laux, P.; Xu, S.; Wang, H.; Yu, Z.; Kunstmann, H. Toward Improved Parameterizations of Reservoir Operation in Ungauged Basins: A Synergistic Framework Coupling Satellite Remote Sensing, Hydrologic Modeling, and Conceptual Operation Schemes. *Water Resour. Res.* **2023**, *59*, e2022WR033026. [CrossRef]
48. Shin, S.; Pokhrel, Y.; Miguez-Macho, G. High-Resolution Modeling of Reservoir Release and Storage Dynamics at the Continental Scale. *Water Resour. Res.* **2019**, *55*, 787–810. [CrossRef]
49. Busker, T.; de Roo, A.; Gelati, E.; Schwatke, C.; Adamovic, M.; Bisselink, B.; Pekel, J.F.; Cottam, A. A global lake and reservoir volume analysis using a surface water dataset and satellite altimetry. *Hydrol. Earth Syst. Sci.* **2019**, *23*, 669–690. [CrossRef]
50. Ali, A.M.; Melsen, L.A.; Teuling, A.J. Inferring reservoir filling strategies under limited-data-availability conditions using hydrological modeling and Earth observations: The case of the Grand Ethiopian Renaissance Dam (GERD). *Hydrol. Earth Syst. Sci.* **2023**, *27*, 4057–4086. [CrossRef]
51. Brunner, M.I.; Naveau, P. Spatial variability in Alpine reservoir regulation: Deriving reservoir operations from streamflow using generalized additive models. *Hydrol. Earth Syst. Sci.* **2023**, *27*, 673–687. [CrossRef]
52. Vu, D.T.; Dang, T.D.; Galelli, S.; Hossain, F. Satellite observations reveal 13 years of reservoir filling strategies, operating rules, and hydrological alterations in the Upper Mekong River basin. *Hydrol. Earth Syst. Sci.* **2022**, *26*, 2345–2364. [CrossRef]
53. Giuliani, M.; Herman, J.D. Modeling the behavior of water reservoir operators via eigenbehavior analysis. *Adv. Water Resour.* **2018**, *122*, 228–237. [CrossRef]
54. Li, Y.; Zhao, G.; Allen, G.H.; Gao, H.L. Diminishing storage returns of reservoir construction. *Nat. Commun.* **2023**, *14*, 3203. [CrossRef]

55. Bonnema, M.; Sikder, S.; Miao, Y.; Chen, X.; Hossain, F.; Ara Pervin, I.; Mahbubur Rahman, S.M.; Lee, H. Understanding satellite-based monthly-to-seasonal reservoir outflow estimation as a function of hydrologic controls. *Water Resour. Res.* **2016**, *52*, 4095–4115. [CrossRef]
56. Lehner, B.; Reidy Liermann, C.; Revenga, C.; Vorosmarty, C.; Fekete, B.; Crouzet, P.; Doll, P.; Endejan, M.; Frenken, K.; Magome, J.; et al. Global Reservoir and Dam Database, Version 1 (GRanDv1): Dams, Revision 01 . 2011. Available online: https://dataverse.harvard.edu/dataset.xhtml?persistentId=doi:10.7910/DVN/GSHD33 (accessed on 30 December 2025).
57. Hanazaki, R.; Yamazaki, D.; Yoshimura, K. Development of a Reservoir Flood Control Scheme for Global Flood Models. *J. Adv. Model. Earth Syst.* **2022**, *14*, e2021MS002944. [CrossRef]
58. Shen, Y.J.; Yamazaki, D.; Pokhrel, Y.; Zhao, G. Improving Global Reservoir Parameterizations by Incorporating Flood Storage Capacity Data and Satellite Observations. *Water Resour. Res.* **2025**, *61*, e2024WR037620. [CrossRef]
59. Lehner, B.; Beames, P.; Mulligan, M.; Zarfl, C.; De Felice, L.; van Soesbergen, A.; Thieme, M.; de Leaniz, C.G.; Anand, M.; Belletti, B.; et al. The Global Dam Watch database of river barrier and reservoir information for large-scale applications. *Sci. Data* **2024**, *11*, 1069. [CrossRef] [PubMed]
60. Zhang, A.T.; Gu, V.X. Global Dam Tracker: A database of more than 35,000 dams with location, catchment, and attribute information. *Sci. Data* **2023**, *10*, 111. [CrossRef]
61. Hawker, L.; Uhe, P.; Paulo, L.; Sosa, J.; Savage, J.; Sampson, C.; Neal, J. A 30 m global map of elevation with forests and buildings removed. *Environ. Res. Lett.* **2022**, *17*, 024016. [CrossRef]
62. Huang, S. *Water Conservancy Gazetteer of Hainan Province (2001–2010)*; Hainan Provincial Local Chronicles; Local Chronicles Publishing House: Haikou, China, 2013; p. 353.
63. Jiang, X.; Ren, F.; Li, Y.; Qiu, W.; Ma, Z.; Cai, Q. Characteristics and Preliminary Causes of Tropical Cyclone Extreme Rainfall Events over Hainan Island. *Adv. Atmos. Sci.* **2018**, *35*, 580–591. [CrossRef]
64. Lehner, B.; Liermann, C.R.; Revenga, C.; Vörömsmarty, C.; Fekete, B.; Crouzet, P.; Döll, P.; Endejan, M.; Frenken, K.; Magome, J.; et al. High-resolution mapping of the world's reservoirs and dams for sustainable river-flow management. *Front. Ecol. Environ.* **2011**, *9*, 494–502. [CrossRef]
65. Schaperow, J.R.; Li, D.; Margulis, S.A.; Lettenmaier, D.P. A near-global, high resolution land surface parameter dataset for the variable infiltration capacity model. *Sci. Data* **2021**, *8*, 216. [CrossRef]
66. Lehner, B.; Verdin, K.; Jarvis, A. New Global Hydrography Derived From Spaceborne Elevation Data. *Eos Trans. Am. Geophys. Union* **2008**, *89*, 93–94. [CrossRef]
67. Huffman, G.J.; Bolvin, D.T.; Joyce, R.; Kelley, O.A.; Nelkin, E.J.; Portier, A.; Stocker, E.F.; Tan, J.; Watters, D.C.; West, B.J. *IMERG V07 Release Notes*; Technical Report; National Aeronautics and Space Administration: Washington, DC, USA, 2024. Available online: https://gpm.nasa.gov/sites/default/files/2024-12/IMERG_V07_ReleaseNotes_241126.pdf (accessed on 30 December 2025).
68. Huffman, G.J.; Bolvin, D.T.; Braithwaite, D.; Hsu, K.-L.; Joyce, R.J.; Kidd, C.; Nelkin, E.J.; Sorooshian, S.; Stocker, E.F.; Tan, J.; et al. Integrated Multi-satellite Retrievals for the Global Precipitation Measurement (GPM) Mission (IMERG). In *Satellite Precipitation Measurement: Volume 1*; Levizzani, V., Kidd, C., Kirschbaum, D.B., Kummerow, C.D., Nakamura, K., Turk, F.J., Eds.; Springer International Publishing: Cham, Switzerland, 2020; pp. 343–353.
69. Shen, Y.; Liu, D.; Jiang, L.; Nielsen, K.; Yin, J.; Liu, J.; Bauer-Gottwein, P. High-resolution water level and storage variation datasets for 338 reservoirs in China during 2010–2021. *Earth Syst. Sci. Data* **2022**, *14*, 5671–5694. [CrossRef]
70. Wing, O.E.J.; Bates, P.D.; Quinn, N.D.; Savage, J.T.S.; Uhe, P.F.; Cooper, A.; Collings, T.P.; Addor, N.; Lord, N.S.; Hatchard, S.; et al. A 30 m Global Flood Inundation Model for Any Climate Scenario. *Water Resour. Res.* **2024**, *60*, e2023WR036460. [CrossRef]
71. Liang, X.; Lettenmaier, D.P.; Wood, E.F.; Burges, S.J. A simple hydrologically based model of land surface water and energy fluxes for general circulation models. *J. Geophys. Res.* **1994**, *99*, 14415–14428. [CrossRef]
72. Wu, H.; Kimball, J.S.; Mantua, N.; Stanford, J. Automated upscaling of river networks for macroscale hydrological modeling. *Water Resour. Res.* **2011**, *47*, W03517. [CrossRef]
73. Wu, H.; Kimball, J.S.; Li, H.; Huang, M.; Leung, L.R.; Adler, R.F. A new global river network database for macroscale hydrologic modeling. *Water Resour. Res.* **2012**, *48*, W09701. [CrossRef]
74. Wu, H.; Li, X.; Schumann, G.J.P.; Alfieri, L.; Chen, Y.; Xu, H.; Wu, Z.; Lu, H.; Hu, Y.; Zhu, Q.; et al. From China's Heavy Precipitation in 2020 to a "Glocal" Hydrometeorological Solution for Flood Risk Prediction. *Adv. Atmos. Sci.* **2021**, *38*, 1–7. [CrossRef]
75. Hu, Y.; Wu, H.; Alfieri, L.; Gu, G.J.; Yilmaz, K.K.; Li, C.Q.; Jiang, L.L.; Huang, Z.J.; Chen, W.T.; Wu, W.; et al. A time-space varying distributed unit hydrograph (TS-DUH) for operational flash flood forecasting using publicly-available datasets. *J. Hydrol.* **2024**, *642*, 131785. [CrossRef]
76. Jiang, L.; Wu, H.; Tao, J.; Kimball, J.S.; Alfieri, L.; Chen, X. Satellite-based evapotranspiration in hydrological model calibration. *Remote Sens.* **2020**, *12*, 428. [CrossRef]
77. Zajac, Z.; Revilla-Romero, B.; Salamon, P.; Burek, P.; Hirpa, F.; Beck, H. The impact of lake and reservoir parameterization on global streamflow simulation. *J. Hydrol.* **2017**, *548*, 552–568. [CrossRef] [PubMed]

78. Dong, N.; Wei, J.; Yang, M.; Yan, D.; Yang, C.; Gao, H.; Arnault, J.; Laux, P.; Zhang, X.; Liu, Y.; et al. Model Estimates of China's Terrestrial Water Storage Variation Due To Reservoir Operation. *Water Resour. Res.* **2022**, *58*, e2021WR031787. [CrossRef]
79. Hou, J.W.; van Dijk, A.I.J.M.; Beck, H.E.; Renzullo, L.J.; Wada, Y. Remotely sensed reservoir water storage dynamics (1984–2015) and the influence of climate variability and management at a global scale. *Hydrol. Earth Syst. Sci.* **2022**, *26*, 3785–3803. [CrossRef]
80. Li, X.; Long, D.; Huang, Q.; Han, P.; Zhao, F.; Wada, Y. High-temporal-resolution water level and storage change data sets for lakes on the Tibetan Plateau during 2000–2017 using multiple altimetric missions and Landsat-derived lake shoreline positions. *Earth Syst. Sci. Data* **2019**, *11*, 1603–1627. [CrossRef]
81. Gao, H. Satellite remote sensing of large lakes and reservoirs: From elevation and area to storage. *Wiley Interdiscip. Rev. Water* **2015**, *2*, 147–157. [CrossRef]
82. Liu, K.; Song, C.; Wang, J.; Ke, L.; Zhu, Y.; Zhu, J.; Ma, R.; Luo, Z. Remote Sensing-Based Modeling of the Bathymetry and Water Storage for Channel-Type Reservoirs Worldwide. *Water Resour. Res.* **2020**, *56*, e2020WR027147. [CrossRef]
83. Fritsch, F.N.; Butland, J. A Method for Constructing Local Monotone Piecewise Cubic Interpolants. *SIAM J. Sci. Stat. Comput.* **1984**, *5*, 300–304. [CrossRef]
84. Kennedy, J.; Eberhart, R. Particle swarm optimization. In Proceedings of the ICNN'95-International Conference on Neural Networks, Perth, WA, Australia, 27 November–1 December 1995; Volume 1944, pp. 1942–1948.
85. Duan, Q.; Sorooshian, S.; Gupta, V. Effective and efficient global optimization for conceptual rainfall-runoff models. *Water Resour. Res.* **1992**, *28*, 1015–1031. [CrossRef]
86. Biswas, N.K.; Hossain, F.; Bonnema, M.; Lee, H.; Chishtie, F. Towards a global Reservoir Assessment Tool for predicting hydrologic impacts and operating patterns of existing and planned reservoirs. *Environ. Model. Softw.* **2021**, *140*, 105043. [CrossRef]
87. Khazaei, B.; Read, L.K.; Casali, M.; Sampson, K.M.; Yates, D.N. GLOBathy, the global lakes bathymetry dataset. *Sci. Data* **2022**, *9*, 36. [CrossRef]
88. Yigzaw, W.; Li, H.Y.; Demissie, Y.; Hejazi, M.I.; Leung, L.R.; Voisin, N.; Payn, R. A New Global Storage-Area-Depth Data Set for Modeling Reservoirs in Land Surface and Earth System Models. *Water Resour. Res.* **2018**, *54*, 10372–10386. [CrossRef]
89. Hao, Z.; Chen, F.; Jia, X.F.; Cai, X.B.; Yang, C.; Du, Y.; Ling, F. GRDL: A New Global Reservoir Area-Storage-Depth Data Set Derived Through Deep Learning-Based Bathymetry Reconstruction. *Water Resour. Res.* **2024**, *60*, e2023WR035781. [CrossRef]
90. Fassoni-Andrade, A.C.; de Paiva, R.C.D.; Fleischmann, A.S. Lake Topography and Active Storage From Satellite Observations of Flood Frequency. *Water Resour. Res.* **2020**, *56*, e2019WR026362. [CrossRef]
91. Feng, D.; Gleason, C.J. More flow upstream and less flow downstream: The changing form and function of global rivers. *Science* **2024**, *386*, 1305–1311. [CrossRef]
92. Fu, L.L.; Pavelsky, T.; Cretaux, J.F.; Morrow, R.; Farrar, J.T.; Vaze, P.; Sengenes, P.; Vinogradova-Shiffer, N.; Sylvestre-Baron, A.; Picot, N.; et al. The Surface Water and Ocean Topography Mission: A Breakthrough in Radar Remote Sensing of the Ocean and Land Surface Water. *Geophys. Res. Lett.* **2024**, *51*, e2023GL107652. [CrossRef]

Disclaimer/Publisher's Note: The statements, opinions and data contained in all publications are solely those of the individual author(s) and contributor(s) and not of MDPI and/or the editor(s). MDPI and/or the editor(s) disclaim responsibility for any injury to people or property resulting from any ideas, methods, instructions or products referred to in the content.